AGU100 ADVANCING EARTH AND SPACE SCIENCE

JGR

Journal of Geophysical Research: Solid Earth

RESEARCH ARTICLE

10.1029/2017JB015369

Key Points:

- We measured uniaxial reaction-induced stresses generated during gypsum formation via bassanite hydration
- Hydration of bassanite generates stresses due to solid volume increase that are limited by viscous compaction
- Induced stresses are highest when porosity is low and reaction rates are slowing

Supporting Information:

- Supporting Information S1
- Data Set S1

Correspondence to:
R. M. Skarbek,
rskarbek@ldeo.columbia.edu

Citation:
Skarbek, R. M., Savage, H. M., Kelemen, P. B., & Yancopoulos, D. (2018). Competition between crystallization-induced expansion and creep compaction during gypsum formation, and implications for serpentinization. *Journal of Geophysical Research: Solid Earth*, *123*. https://doi.org/10.1029/2017JB015369

Received 19 DEC 2017
Accepted 2 JUN 2018
Accepted article online 9 JUN 2018

Competition Between Crystallization-Induced Expansion and Creep Compaction During Gypsum Formation, and Implications for Serpentinization

Rob M. Skarbek[1], **Heather M. Savage**[1], **Peter B. Kelemen**[1], **and Demetra Yancopoulos**[1]

[1]Lamont-Doherty Earth Observatory, Columbia University, Palisades, NY, USA

Abstract Deformation caused by reaction-driven volume increases is an important process in many geological settings. The interaction of rocks with reactive fluids can change permeability and reactive surface area, leading to a large variety of feedbacks. Gypsum ($CaSO_4 \cdot 2H_2O$) is an ideal material to study these processes. It forms rapidly at room temperature via bassanite ($CaSO_4 \cdot [1/2]H_2O$) hydration and is commonly used as an analog for rocks in high-temperature, high-pressure conditions. We conducted uniaxial deformation experiments on porous bassanite aggregates to study the effects of applied axial load σ_a on deformation during the formation of gypsum. While hydration of bassanite involves a solid volume increase, gypsum exhibits significant creep compaction when in contact with water. These two processes occur simultaneously. Samples exhibited an initial phase of deformation followed by a slower secondary phase. A particular value of σ_a separates expansion from compaction during each of the deformation phases. At $\sigma_a \leq 150$ kPa, samples expanded initially; for $\sigma_a \geq 230$ kPa, samples compacted initially. Up to $\sigma_a \approx 3.2$ MPa, samples expanded after compacting initially, while for $\sigma_a \geq 3.6$ MPa, no further deformation or continued compaction occurred. This behavior implies that crystallization-induced stresses depend on porosity and reaction extent such that larger stresses cannot be generated by the reaction. We explain aspects of the observed behavior with a model that predicts strain evolution using kinetic relationships for the reaction and creep rates and consider the implications of our results for reaction-induced fracturing during serpentinization.

1. Introduction

Porous materials can be subjected to significant stresses when crystals precipitate from liquid contained within pores. This process, referred to here as *confined crystallization*, can cause serious damage to building materials, induce fracturing or viscous flow in the host material, and lead to large changes in permeability in geologic environments. A necessary condition for the growth of crystals confined within pores is the existence of a thin fluid film at grain contacts. The presence of such a film allows for crystal growth against external confining stresses and leads to the thermodynamic concept of “crystallization pressure”—that is, the pressure a growing crystal is capable of exerting on contacting surfaces.

The generation of stress due to confined crystallization is a subject that has received considerable attention by authors with engineering applications in mind. The crystallization of salts is a well-documented source of deterioration in building stones (e.g., Li, 2017; Novak & Colville, 1989), tunnel walls (Anagnostou et al., 2010), and oil and gas wellbores (e.g., Ghofrani & Plack, 1993; Wolterbeek et al., 2017). Crystallization in these types of environments frequently occurs in unsaturated conditions, where both a fluid and a vapor phase are present in pores. Numerous experimental (e.g., Noiriel et al., 2010; Tsui et al., 2003; Wolterbeek et al., 2017) and theoretical (e.g., Coussy, 2006; Flatt, 2002; Scherer, 1999, 2004; Serafeimidis & Anagnostou, 2014; Steiger, 2005a, 2005b) studies have been conducted in attempts to quantify the stresses involved, mostly in systems where crystallization occurs within a porous medium whose matrix does not participate in the reaction.

In problems of geologic interest a porous rock matrix can supply reactive components via dissolution that can precipitate within the pore space (Putnis, 2009, 2015). Such reactions are commonly referred to as *replacement reactions*. When confined crystallization takes place during a replacement reaction, it can generate crystallization pressure if the molar volume of the product phase is larger than that of the parent phase, for example, during mineral hydration, carbonation, or oxidation reactions (Kelemen et al., 2011; Kelemen & Hirth, 2012).

Relatively little work has been done to constrain crystallization pressures in these types of situations (see Ghofrani & Plack, 1993; Ostapenko, 1976; Ostapenko & Yaroshenko, 1975; van Noort et al., 2017; Wolterbeek et al., 2017). However, the role of confined crystallization is of primary importance to the dynamics of numerous geophysical processes, including replacement of olivine by serpentinite or magnesite (Kelemen et al., 2011; Kelemen & Hirth, 2012), reaction-induced fracturing (Kuleci et al., 2017; Zhu et al., 2016), and geologic carbon sequestration (Kelemen & Matter, 2008; Matter & Kelemen, 2009).

In this work we present the results of experiments that enable measurements of crystallization-induced stress and deformation due to the in situ formation of gypsum ($CaSO_4 \cdot 2H_2O$) from bassanite ($CaSO_4 \cdot [1/2]H_2O$) in samples with ~30% initial porosity. We identify two regimes of deformation and show that confined crystallization in this system can generate stresses up to 150–230 kPa at high initial porosities (~30%) and ~3.6 MPa at low porosities (<10%). We discuss the observed deformation in terms of a competition between reaction-induced volume expansion and creep-induced compaction and show that the main features of our results can be explained with a simple phenomenological model that takes these processes into account. Finally, we draw comparisons between hydration of bassanite and hydration of olivine and discuss the implications of our results for reaction-induced fracturing during serpentinization.

2. Background

2.1. Bassanite Hydration

Our focus is the hydration of bassanite (calcium sulphate hemihydrate) to form gypsum (calcium sulphate dihydrate) via the reaction

$$CaSO_4 \cdot \frac{1}{2}H_2O + \frac{3}{2}H_2O = CaSO_4 \cdot 2H_2O. \tag{1}$$

Bassanite is commonly known as plaster of Paris; when mixed with water it sets to form gypsum plaster, a common building material (e.g., Charola et al., 2007). Gypsum is also a common mineral, being frequently found in evaporite sequences (Warren, 2006) and is one of the weakest materials found in the Earth's crust (Heard & Rubey, 1966). Additionally, the dehydration of gypsum is frequently studied as an analog for reactions that occur at higher temperatures and pressures (e.g., serpentinization). Thus, the properties of reaction (1) have received study both for engineering purposes (e.g., Hand, 1997; Singh & Middendorf, 2007; Van Driessche et al., 2017) and for geologic problems (e.g., Brantut et al., 2012; Llana-Fúnez et al., 2012; Wong et al., 1997).

Bassanite hydration occurs through a dissolution-precipitation mechanism (Fujii & Kondo, 1986; Ridge et al., 1972; Schiller, 1974; Van Rosmalen et al., 1981). Because bassanite is more soluble in water than gypsum, ~0.07 M versus ~0.015 M in pure water at room temperature and atmospheric pressure (Azimi et al., 2007; Van Driessche et al., 2017), a fluid that is saturated with respect to bassanite is supersaturated with respect to gypsum, and gypsum will precipitate (e.g., Hand, 1994; Singh & Middendorf, 2007). Numerous kinetic expressions for the rate of bassanite hydration have been proposed based on the dissolution-precipitation mechanism (see Carlson & Taavitsainen, 2008; Hand, 1994; Singh & Middendorf, 2007). In this paper, we adopt the kinetic model of Carlson and Taavitsainen (2008), who measured reaction rates at room temperature using the attenuation of ultrasonic transmissions through a reacting sample of bassanite paste, finding

$$\dot{\alpha} = K_\alpha (1 - \alpha)^2, \tag{2}$$

where α is the reaction extent such that $0 < \alpha < 1$ and K_α is an empirical constant with a value of 2.16×10^{-4} s^{-1}.

The bassanite hydration reaction is fast, equation (2) predicts full conversion in ~2 hr. Most studies on the kinetics of reaction (1) do not consider temperature dependence of the reaction rate (see Hand, 1994; Singh & Middendorf, 2007), although some evidence indicates that it is fastest at 35°C (Comel et al., 1979). Accordingly, we do not consider temperature effects in our experiments, which were all performed at room temperature.

2.2. Crystallization Pressure

When a precipitation reaction occurs in the void space of a porous material, it is possible for the growth of the product crystals to exert a stress on grain-to-grain contact surfaces. A fluid film must necessarily be present between the grain surfaces for the stress-generating reaction to occur (Ostapenko & Yaroshenko, 1975; Steiger, 2005a). The thickness of the fluid film may be on the order of few tens of nanometers or less

(Scherer, 1999) and must also be supersaturated with respect to the product phase for precipitation to proceed. Additionally, for precipitation of hydrated minerals the fluid film must be in contact with the pore water, as fluid mass in the intergranular film will be taken up by the hydration reaction and must be replenished for further progress. Finally, for in situ replacement reactions, the molar volume of the product phase must be larger than that of the parent phase; otherwise, reaction progress would tend to increase porosity and result in fewer grain-to-grain contacts (Putnis, 2015).

If an external confining stress σ is applied to a fluid-saturated porous material with pore fluid pressure p_p, the solid grains will support an effective stress of $\sigma' = \sigma - p_p$. It follows that in mechanical equilibrium, the stress supported between grain contacts through an intergranular fluid film must be equal to σ'. However, in fluid films narrower than ∼100 nm, a so-called *disjoining pressure* is present, that is, due to the combined effects of electrostatic interactions, Van der Waals forces, and forces resulting from structural changes in hydrogen bonds within water molecules very near the grain surfaces (Derjaguin, 1987; Gonçalvès et al., 2010; Marčelja & Radiá, 1976).

The disjoining pressure is not strictly a "pressure" in that it is defined as a tensor field rather than as a scalar, so that there are two unequal components that act normal and tangential to grain boundary surfaces (Derjaguin, 1987). Denoting the normal component as π_D, the normal stress felt by grain boundaries adjacent to the fluid film is $p_p + \pi_D$. The disjoining pressure plays no direct role in fluid flow, so that gradients in p_p drive flow as usual (e.g., Rousseau-Gueutin et al., 2009).

It is the presence of the intergranular fluid layer and the disjoining pressure that enable a crystallization pressure to develop, and there have been numerous attempts at formulating a theoretical expression to predict its value. Most attention has focused on drying-induced salt crystallization in porous building materials. An expression proposed by Correns (1949) relates the crystallization pressure Δp to the extent of supersaturation of pore fluid with respect to a given solute as (see also Flatt et al., 2007)

$$\Delta p = \frac{RT}{V_c}\ln\left(\frac{x}{x_0}\right), \tag{3}$$

where R is the ideal gas constant, T is temperature, V_c is the molar volume of the crystallizing solid, and x/x_0 is the solute concentration in a supersaturated solution relative to that in a saturated solution. Similar expressions appear in the works of Weyl (1959) and de Boer (1977). Steiger (2005a) pointed out that equation (3) is correct only for ideal solutions in which a growing crystal forms through precipitation of a single fluid component.

A more complete equation for Δp, allowing for nonideal solutions, crystallization from multiple components, and taking into account the surface energy of the crystal-liquid interface was given by Steiger (2005b)

$$\Delta p = \frac{\nu_c RT}{V_c}\left[\ln\left(\frac{m}{m_0}\right) + \ln\left(\frac{\gamma_\pm}{\gamma_{\pm,0}}\right) + \frac{\nu_w}{\nu_c}\ln\left(\frac{a_w}{a_{w,0}}\right)\right] - \gamma_{\mathrm{cl}}\kappa_{cl}, \tag{4}$$

where ν_c and ν_w are the stoichiometric constants of the crystal and water, m/m_0 is the molality of the solution relative to that of a saturated solution, and γ_{cl} and κ_{cl} are the free energy and curvature of the crystal-liquid interface. The second and third terms in the brackets account for nonideal behavior of the solution, where $\gamma_\pm/\gamma_{\pm,0}$ and $a_{\mathrm{w}}/a_{\mathrm{w},0}$ are the mean activity coefficient of the solution and the water activity relative to saturated states, respectively (Steiger, 2005a). The final term accounts for the surface energy of the growing crystal, which becomes important for crystals smaller than 0.1 – 1 μm (Steiger, 2005b). Both equations (3) and (4) ignore the effects of strain-induced changes in molar solid volume, which should be small for applied loads up to 0.1 – 1 GPa depending on the bulk modulus of the crystal (Steiger, 2005a; Wolterbeek et al., 2017). Equation (4) reduces to equation (3) for crystallization of a single component ($\nu_{\mathrm{c}} = 1$), anhydrous ($\nu_{\mathrm{w}} = 0$) salt from an ideal solution ($\gamma_\pm/\gamma_{\pm,0} = 1$; Steiger, 2005a).

When crystallization takes places in an unsaturated medium, the presence of a liquid-vapor interface will affect the crystallization pressure, because the liquid must be in equilibrium with both the precipitating solid and the vapor phase (Coussy, 2006; Scherer, 2000). Coussy (2006) considered such a situation, allowing for nonideal behavior of the solute, but not the solvent, and found

$$\Delta p = \frac{\nu_{\mathrm{c}} RT}{V_c}\left[\ln\left(\frac{x}{x_0}\right) + \frac{\nu_{\mathrm{w}}}{\nu_{\mathrm{c}}}\ln\left(\frac{x_{\mathrm{w}}}{x_{\mathrm{w},0}}\right)\right] + \delta\gamma_{\mathrm{lv}}\kappa_{\mathrm{lv}}, \tag{5}$$

where δ is a dimensionless constant accounting for volume change in the solution fluid due to crystallization and $x_\mathrm{w}/x_{\mathrm{w},0}$ is the mole fraction of water in the solution relative to the saturated state. Similar to equation (4), the final term accounts for the surface energy in the liquid-vapor interface. Scherer (2000) derived a similar equation for an ideal solution. When interfacial effects are ignored, equations (5) and (4) are equivalent for ideal behavior in the solvent (i.e., $a_w/a_{w,0} = x_\mathrm{w}/x_{\mathrm{w},0}$). When the liquid-vapor interface is ignored, equation (5) is also equivalent to an expression derived by Flatt (2002). To our knowledge, no derivation for the crystallization pressure has been published that takes all of the effects mentioned in this section into account. However, comparison of equations (4) and (5) suggests adding the term $\delta\gamma_\mathrm{lv}\kappa_\mathrm{lv}$ to equation (4) (e.g., Espinosa-Marzal & Scherer, 2010).

In all of the treatments that lead to equations (3)–(5), the porous skeleton does not react with the pore fluid. Crystallization is considered to have taken place in pores through precipitation of externally derived solute components, as in the invasion of building material by a salted solution. Kelemen et al. (2011) pointed out that equation (4) can be written in terms of the change in the Gibbs free energy ΔG_r of the reaction (see also Kelemen & Hirth, 2012; Ostapenko, 1976) and argued that V_c should be replaced with the change in molar volume ΔV_s between the solid products and solid reactants for an in situ replacement reaction, in which case

$$\Delta p = -\frac{\Delta G_r}{\Delta V_s}. \tag{6}$$

Equation (6) is a maximum bound on Δp, since changes in entropy and release of heat due to hydration and crystallization from fluid will reduce the energy available for mechanical work against an applied load (Kelemen & Hirth, 2012). Wolterbeek et al. (2017) generalized equation (6) to include the effects of dissolved components present in the solution phase. However, equation (6) serves as a good estimate when the mass of dissolved material is small relative to the mass of precipitated material, as should be the case when both the solubility of the product phase and the porosity are small (Kelemen & Hirth, 2012; Wolterbeek et al., 2017).

The free energy of reaction (1) as a function of temperature T and fluid pressure p_f was calculated by Llana-Fúnez et al. (2012) as

$$\Delta G_r = 3591.06 - 529.253T - 0.0775T^2 + 92.705T\ln(T) - 5\times10^{-6}p_f^3 + 5.54\times10^{-3}p_f^2 + 6.8665p_f, \tag{7}$$

with free energy in J/mol, pressure in MPa, and temperature in K. At room temperature and the range of applied loads that we studied (12 kPa–4 MPa), equation (7) along with equation (6) predicts $\Delta p \approx 185$ MPa for bassanite hydration.

As for the theoretical studies mentioned above, most experimental studies have been for systems where the porous matrix does not react, but there have been a few studies that examined reactive porous materials. Experiments generally consist of a setup to apply a uniaxial load to a reacting porous aggregate and record strain as the reaction proceeds. A maximum crystallization-induced stress σ_c can then be determined by conducting experiments at different loads and choosing the load where strain transitions from expansion to compaction.

Ostapenko and Yaroshenko (1975) performed experiments on the hydration of porous samples of bassanite and lime (CaO) and measured crystallization-induced stresses of 4.9 and 49 MPa, respectively. In a similar study, Ostapenko (1976) recorded stresses generated during hydration of porous periclase (MgO) of 20–200 MPa. Recently, Wolterbeek et al. (2017) observed an induced stress due to hydration of porous lime of ~150 MPa. Experimentally recorded values of crystallization-induced stress, along with the corresponding crystallization pressure predicted using equation (6), are collected in Table 1. All experimental estimates are 1 to 2 orders of magnitude smaller than the thermodynamically predicted Δp. We have excluded results obtained from more complicated reaction pathways such as for the hydration of industrial cement powders (e.g., Ghofrani & Plack, 1993).

The experimental results in Table 1 are not measurements of the crystallization pressure but rather are measurements of a crystallization-induced stress. The induced stress depends on the constitutive properties of the porous aggregate formed by the product and reactant grains (porosity, elastic, inelastic properties of pure solids, grain size, etc.). The crystallization pressure, as predicted for example by equation (6), depends on thermodynamic properties and is a measure of the chemical potential energy available to be converted into stress (Kelemen & Hirth, 2012).

Table 1
Comparison of Experimentally Measured and Theoretically Predicted Values of Crystallization Pressure for Specific Reactions

Reaction	σ_c measured (MPa)	Δp predicted (MPa)
$CaSO_4 \cdot \frac{1}{2}H_2O + \frac{3}{2}H_2O \rightarrow CaSO_4 \cdot 2H_2O$	4.9[a], 3.6[b], 0.15 − 0.23[b]	185
$CaO + H_2O \rightarrow Ca(OH)_2$	49[a], 153[c]	3,400
$MgO + H_2O \rightarrow Mg(OH)_2$	20–200[d]	2,000

[a] Ostapenko and Yaroshenko (1975). [b] This study. [c] Wolterbeek et al. (2017). [d] Ostapenko (1976).

Dispersed crystallization in a porous material produces a mean tensile stress that can act against an applied load (Coussy, 2006). Crystallization-induced stresses approaching Δp would only be observed if a reacting porous aggregate can withstand a tensile stress of that magnitude without failing. However, predicted values of Δp are in general much larger than values of rock strength and so failure, either through dilatant fracture or inelastic yielding, should be expected at much lower stresses, as is the case.

3. Methods

The starting material used for fabricating samples was 97% pure bassanite powder or 98% pure gypsum powder purchased from Fischer Scientific. The grain size d measured by sieving for both of these materials is in the range 63 μm $< d <$ 250 μm. Approximately 5 g of powder was cold pressed in a steel die with a diameter of 1.22 cm. The inside of the pressing die, as well as the pressing piston, was coated with a thin film of teflon lubrication to prevent the pressed samples from getting stuck inside the die and potentially fracturing during removal. Bassanite powder was pressed at an axial load σ_a of 10 MPa for 10 min, which produced intact, cylindrical samples with initial heights $h_i = 2.5–2.6$ cm and porosities $\phi_i \approx 0.3$. Gypsum powder was pressed at $\sigma_a = 5$ MPa for 10 min, producing samples with $h_i = 2.6–2.9$ cm and $\phi_i \approx 0.23$. Individual sample properties including the initial mass m_i are listed in Table 2. Precompaction stresses larger than 10 MPa for bassanite, or 5 MPa for gypsum, generally produced cracked specimens.

Experimental runs were conducted in a separate die with an identical diameter to that of the pressing die. The experimental die was placed in a brass pan, with the bottom opening of the die covered by a porous steel

Table 2
Summary of Sample Properties and Results for Individual Experiments

Exp. #	σ_a (kPa)	m_i (g)	m_{fdry} (g)	m_{fwet} (g)	h_i (mm)	h_r (mm)	h_p (mm)	ϕ_i (%)	ϕ_r (%)	α_r	ϵ_{40} (%)
B21	502	5.5826(1)	6.3401(1)	6.4956(1)	25.43(1)	21.59(8)	0	30.2(1)	5.2(3)	0.791(3)	−0.64
B22	12	5.6335(1)	6.4289(1)	6.6659(1)	25.63(1)	23.07(8)	0	30.3(1)	7.7(4)	0.822(3)	2.30
B24	502	5.5136(1)	6.3216(1)	6.4802(1)	25.09(1)	22.68(8)	0	30.2(1)	5.4(3)	0.854(3)	−0.27
B25	2024	5.5697(1)	5.9966(1)	6.1107(1)	25.42(1)	13.76(5)	9.28(2)	30.0(1)	4.7(4)	0.880(3)	−2.75
B26	330	5.6609(1)	6.4097(1)	6.5878(1)	25.76(1)	21.76(8)	9.60(1)	30.3(1)	5.3(3)	0.947(3)	−0.03
B27	230	5.4182(1)	6.1962(1)	6.3680(1)	24.77(1)	21.89(8)	0	30.5(1)	5.9(3)	0.837(3)	0.21
B28	150	5.6005(1)	6.4370(1)	6.6543(1)	25.50(1)	24.20(8)	0	30.3(1)	7.2(4)	0.870(3)	0.92
B29	12	5.6759(1)	6.5016(1)	6.7649(1)	25.72(1)	24.42(9)	0	30.0(1)	8.5(4)	0.848(3)	2.46
B30	12	5.7223(1)	6.5299(1)	6.7659(1)	26.10(1)	23.16(8)	0	30.5(1)	7.5(4)	0.822(3)	2.48
B31	2024	5.5446(1)	6.1232(1)	6.2744(1)	25.05(1)	18.57(7)	10.84(8)	29.8(1)	9.3(4)	0.781(3)	−2.59
B32	3928	5.6306(1)	6.0308(1)	6.0987(1)	25.67(1)	12.40(6)	3.96(9)	30.5(1)	3.0(3)	0.760(3)	−4.82
B33	3166	5.7065(1)	6.2608(1)	6.3538(1)	25.99(1)	16.89(6)	11.44(6)	30.4(1)	1.6(2)	0.928(3)	−4.31
B34	3553	5.8214(1)	6.3146(1)	6.3903(1)	26.48(1)	14.94(6)	13.63(9)	30.2(1)	−0.3(6)	0.934(3)	−4.10
B35	3928	5.0000(1)	—	—	27.83(1)	—	—	30.0(1)	—	—	−0.10
G11	12	5.4167(1)	—	—	26.24(1)	—	—	23.0(1)	—	—	−0.51
G12	2024	5.8260(1)	—	—	28.86(1)	—	—	23.3(1)	—	—	−4.04

Note. Experiments on bassanite are labeled as B##, precompacted at 10 MPa; those on gypsum are labeled as G##, precompacted at 5 MP. Symbols used: σ_a = axial load; m_i = initial mass; m_{fdry} = final mass after drying; m_{fwet} = final mass with pore water; h_i = initial height; h_r = thickness of reacted region; h_p = thickness of transition zone; ϕ_i = initial porosity; ϕ_r = porosity of reacted region; α = reaction extent; ϵ_{40} = axial strain after 40 hr.

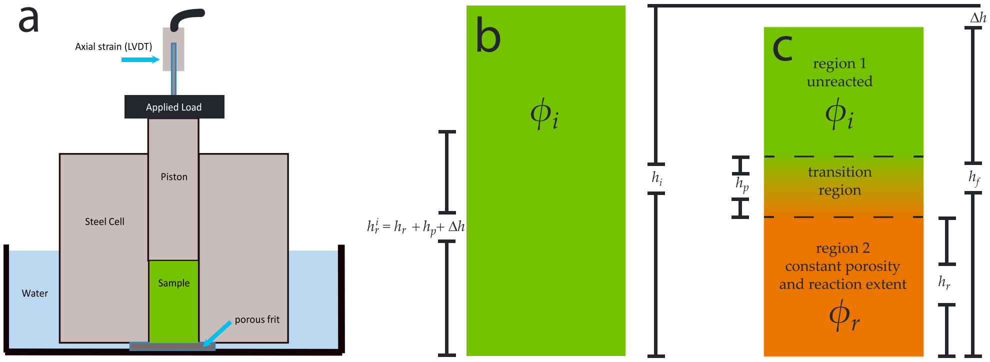

Figure 1. (a) Schematic cartoon of experimental setup. Schematic cartoon of a sample (b) before and (c) after a hydration experiment. LVDT = linear variable displacement transformer.

frit (see Figure 1a). The sample was then placed into the die, and a dead-weight axial load was applied via a piston placed into the die on top of the sample. Finally, the pan was filled with 1 L of water and then covered, marking the beginning of the experiment. Adding 1 L of water resulted in a fluid pressure at the base of the sample of ~350 Pa. Samples began to react almost immediately in most cases. During the entire experiment, the displacement of the axial piston was measured with a linear variable displacement transformer with a range of ±1.27 cm.

At the end of experimental runs, wet samples were removed from the die and the height $h_{f\mathrm{Wet}}$ and mass $m_{f\mathrm{Wet}}$ were recorded. Samples were then dried at 40°C in an 85-kPa vacuum. We performed drying experiments on pure gypsum powder and did not observed any significant change in mass at these conditions. During drying, the samples were periodically removed from the drying oven to record the mass, and the drying process was stopped when the mass of the sample was found to be changing by less than 1% over a 24-hr period. The entire drying process took 2–3 days. When samples were determined to have been fully dried, the height $h_{f\mathrm{Dry}}$ and mass $m_{f\mathrm{Dry}}$ were recorded a final time (see Table 2).

Once fully dried, samples were epoxied and sliced into axial cross sections. We scanned the cross sections at high resolution and performed a simple analysis (see supporting information for details) on the resulting images to determine the thickness of reacted, unreacted, and transitional regions inside the samples (Figures S1–S5).

The measurement of strain during an experiment, as well as the mass changes and the thickness of the reacted regions after an experiment, allows for calculation of the extent of the reaction, as well as the porosity within the reacted region. Figures 1b and 1c show a schematic cartoon of a sample before and after an experiment, where the total sample height has decreased by an amount Δh. Based on the image analysis, we assume that samples consist of a reacted region (Region 2) of height h_r with constant porosity $\phi_r \leq \phi_i$ and reaction extent $\alpha_r \leq 1$, separated from unreacted material (Region 1) by a transition region of thickness h_p. Inside the transition region we assume that porosity and reaction extent change linearly from $\phi = \phi_r$ and $\alpha = \alpha_r$ at $h = h_r$, to $\phi = \phi_i$ and $\alpha = 0$ at $h = h_r + h_p$. Furthermore, we assume that all of the change in sample height occurs due to deformation in the reacted region, so that the unreacted part of the sample is effectively rigid throughout the course of the experiment, which is supported by an experiment on a dry bassanite sample (section 5.1) and recent deformation experiments on porous bassanite Bedford et al. (2018). Then the height of the reacted and transition regions together at the start of the experiment may be written as $h_r^i = h_r + h_p + \Delta h$. Finally, the existence of an unreacted region in any sample implies that this region is completely unsaturated, otherwise it would have reacted. Thus, we assume that at the end of an experiment, Region 2 is completely saturated and Region 1 completely dry, and that in the transition region the saturation decreases linearly between the two values. Because we cannot independently measure spatial variations of porosity or reaction extent within the samples, the assumptions detailed here will necessarily lead to errors in the estimated values.

These assumptions lead to the conclusion that any pore water in the sample is contained entirely within the reacted region. Then ϕ_r can be estimated from the volume of water contained in the sample at the end of the experiment

$$V_w = \frac{m_{f\mathrm{Wet}} - m_{f\mathrm{Dry}}}{\rho_w} = \pi r^2 \left[\phi_r h_r + \left(\frac{\phi_i + 2\phi_r}{6} \right) h_p \right], \tag{8}$$

where ρ_w is the density of water at room temperature and r is the radius of the experimental die. Additionally, if all of the deformation and mass change in the sample occurred in the reacted region, then the mass of this region at the beginning of the experiment is

$$m_r^i = \pi r^2 \rho_i h_r^i = \pi r^2 \rho_i (h_r + h_p + \Delta h), \tag{9}$$

where ρ_i is the initial bulk density of the sample. The reaction extent can be estimated from the stoichiometry of the reaction and the change in mass $(m_{f\mathrm{Dry}} - m_i)$ of the reacted region as

$$\alpha_r = \frac{(m_{f\mathrm{Dry}} - m_i) M_{\mathrm{B}}}{m_r^i (M_{\mathrm{G}} - M_{\mathrm{B}})}, \tag{10}$$

where $M_{\mathrm{B}} = 146.9492$ g/mol and $M_{\mathrm{G}} = 172.172$ g/mol denote the molar masses of bassanite and gypsum, respectively. Additionally, we compute the mean values of porosity $\overline{\phi}$ and reaction extent $\overline{\alpha}$ in the combined reacted and transition zones as

$$\overline{\alpha} = \left[\frac{2h_r + h_p}{2(h_r + h_p)} \right] \alpha_r, \tag{11}$$

and

$$\overline{\phi} = \frac{2\phi_r h_r + (\phi_r + \phi_i) h_p}{2(H_r + h_p)}. \tag{12}$$

4. Results

We performed three sets of experiments. The main set of experiments was conducted on hydrating bassanite samples as described above. In addition, we performed a single experiment on a dry bassanite sample in an identical setup as the main set of experiments, except that no water was introduced to the sample. The dry experiment was conducted at the largest axial load subjected to the reacting samples and serves to illustrate that little deformation takes place in the dry regions of the hydrated bassanite samples. We also performed two experiments on cold-pressed gypsum samples that were otherwise identical to experiments on bassanite samples. The gypsum experiments enable an estimate of the amount of creep compaction that occurs in the product gypsum phase during bassanite hydration experiments. All experimental data are contained in Data Set S1.

4.1. Experiments on Bassanite

Axial strain data from all experiments on bassanite samples are shown in Figure 2. We report axial strain as $\epsilon_a = \Delta h / h_i$ and define positive strain as expansion relative to the initial sample height h_i. The applied axial loads range from ~12 to 3,926 kPa (Table 2). Fluctuations appear in the strain data near the end of some experiments, particularly samples B26 and B29, when the samples have largely stopped deforming. These are due to sensitivity of the linear variable displacement transformer to daily changes in the room temperature, on the order of 3 μm/°C. Note that time is plotted on a logarithmic scale in Figure 2, so these fluctuations occur over longer times than may at first be apparent.

In most of the experiments, measurable strain starts to develop within 2 min after introducing the water. Two experiments (B22 $\sigma_a = 12$ kPa and B33 $\sigma_a = 3,166$ kPa) did not begin to develop measurable strain until over an hour after the addition of water. For ease of comparison with the other experiments, the axial strain data for B22 and B33 have been shifted by 15,015 and 4,715 s, respectively.

The samples exhibit a variety of behaviors, but in general there is a relatively fast, initial phase of deformation followed by a slower secondary phase. The exception is sample B35 ($\sigma_a = 3,926$ kPa) without any water. Expansion during the initial phase only occurred in samples subjected to axial loads $\sigma_a \leq 150$ kPa (B22, B28, B29, and B30). All other samples compacted initially, so that the change from initial expansion to initial compaction occurs in the range 150 kPa $< \sigma_a <$ 230 kPa.

Expansion after the initial phase of compaction occurred in samples subjected to loads in the range 230–3,166 kPa (B21, B24, B26, B27, B31, and B33), with the exception of B25. For $\sigma_a = 330$ kPa (B26) and

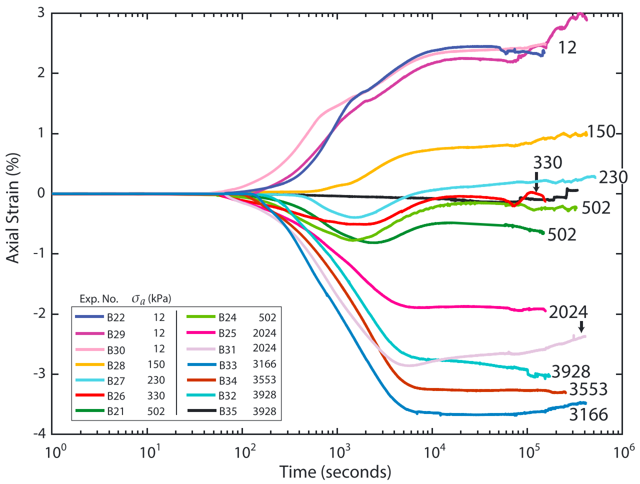

Figure 2. Axial strain data for all bassanite hydration experiments, computed as $\epsilon_a = \Delta h/h_i$. The legend shows the experiment number by color, along with the applied axial load σ_a in kPa. No water was added to experiment B35. See Table 2 for parameters corresponding to each experiment number.

$\sigma_a = 502$ kPa (B21 and B24), a final phase of very slow compaction occurred. Sample B27 monotonically expanded after initial compaction and resulted in net expansion at the largest axial load (230 kPa) that we observed.

The boundary between secondary expansion and compaction is located at $\sigma_a = 3,553$ kPa (B34), where essentially no deformation was observed after initial compaction. Sample B25 was anomalous in that it also did not deform after initial compaction at $\sigma_a = 2,024$ kPa, while sample B31 expanded considerably after compaction under the same load. The only sample that compacted directly after initial compaction was B32 at $\sigma_a = 3,926$ kPa.

Figure 3a shows the thicknesses of the reacted h_r (triangles) and its combined thickness $h_r + h_p$ with the transition (diamonds) region observed in the samples, normalized by the final total height h_f. Values are listed in Table 2. In samples with no visible transition region (i.e., $h_p = 0$), $h_r = h_f$. Except for sample B26 ($\sigma_a = 330$ kPa), transition regions are not observed at axial loads $\sigma_a \leq 502$ kPa. Additionally, unreacted material is only observed at axial loads $\sigma_a \geq 2,024$ kPa. Generally, the thickness of the reacted and transition regions together $h_r + h_p$ encompasses the entire sample up to $\sigma_a = 2,024$ kPa and then begins to decrease with increasing load, reaching only ~0.6 h_f at $\sigma_a = 3,928$ kPa.

Figure 3b shows the estimated reaction extent α_r in the reacted region (circles). These values fall in the range 0.75–0.95 and do not show any obvious trend with applied load. Figure 3b also shows the mean reaction extent $\overline{\alpha}$ in the reacted and transition regions combined (squares) and gives a measure of the total amount of reacted material in samples where a transition region was observed. These values, combined with the values

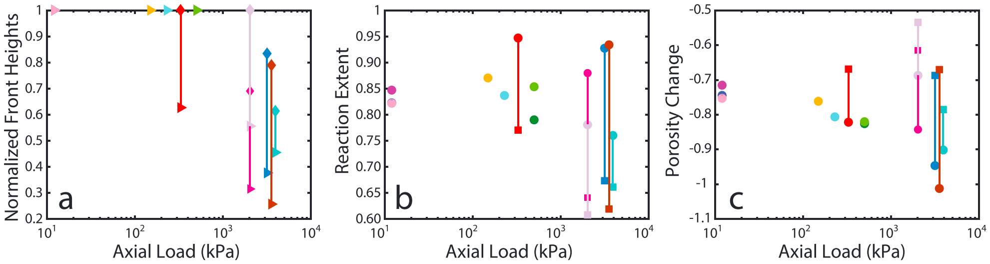

Figure 3. (a) Thicknesses of the reacted region h_r (triangles) and its combined thickness $h_r + h_p$ with the transition (diamonds) region, normalized by the final total height h_f. (b) Estimated reaction extent α_r in the reacted region (circles) and mean reaction extent $\overline{\alpha}$ in the reacted and transition regions combined (squares). (c) Change in porosity $\phi_r - \phi_i$ in the reacted region (circles), normalized by the initial porosity, and normalized change in mean porosity $\overline{\phi} - \phi_i$ in the reacted and transition regions combined (squares). Colors are as in Figure 2.

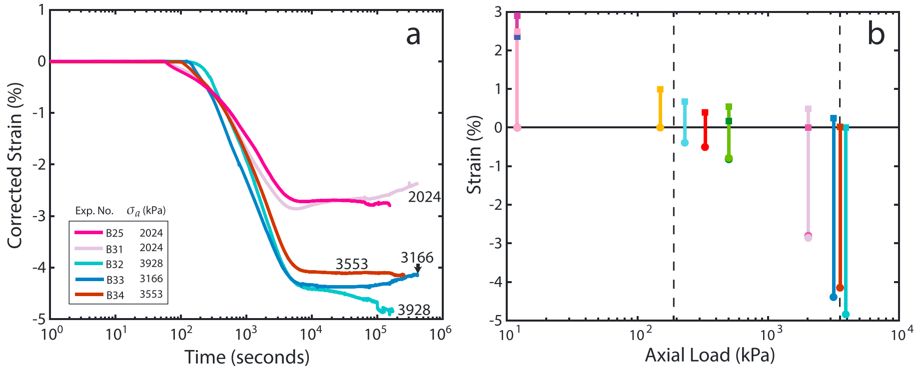

Figure 4. (a) Corrected axial strain data for bassanite hydration experiments with axial load $\sigma_a \geq 2$ MPa, computed as $\epsilon'_a = \Delta h/h^r_i$. (b) Minimum strain (circles) and the difference between the final and minimum strains (squares) for each experiment. Colors are as in Figure 2.

of α_r for samples without a transition region, show a general decrease with increasing load, from 0.77 to 0.87 at loads up to 502 kPa, falling to 0.61 to 0.67 at higher loads.

Estimates of the change in porosity $\phi_r - \phi_i$ in the reacted region (circles), normalized by the initial porosity, are shown in Figure 3c. There is a general log linear increase in the magnitude of porosity change with increasing load, although sample B31 ($\sigma_a = 2,024$ kPa) deviates from the observed trend. The magnitude of the porosity decrease increases from 70% to 80% at $\sigma_a = 12$ kPa, to 90% to 100% at the highest loads. As for the reaction extent, Figure 3c also shows the normalized change in mean porosity $\overline{\phi} - \phi_i$ in the reacted and transition regions combined (squares). The magnitude of the porosity change when considering these two regions together is between 10% and 30% larger than the change in just the reacted region, since the porosity in the transition region increases toward ϕ_i at $h_r + h_p$.

In samples with unreacted regions, computing strain relative to the total initial height as in Figure 2 underestimates the actual strain in the reacted and transition regions, since only material with an initial height $h^i_r = h_r + h_p + \Delta h$ deformed. A corrected strain, defined as $\epsilon'_a = \Delta h/h^i_r$, serves as a more accurate measure of strain in these samples. However, uncertainties in the location of h_p will introduce uncertainty into the value of ϵ'_a. The corrected strains for these experiments (B25, B31–B34, $\sigma_a = 2,024$–$3,928$ kPa), shown in Figure 4a, illustrate that the magnitude of the corrected strain generally becomes larger with increasing axial load as should be expected, whereas the uncorrected strain data in Figure 2 do not show this behavior for $\sigma_a \geq 2,024$ kPa.

The strain results are summarized in Figure 4b, which shows the minimum strains (circles), as well as the difference between the minimum and final strains (squares) for each experiment as a function the applied load. For experiments that experienced only expansion ($\sigma_a \leq 150$ kPa), the minimum strain is 0. For experiments that compacted initially, but then expanded (230 kPa $\leq \sigma_a \leq 3,166$ kPa, with the exception of B25 at $\sigma_a = 2,024$ kPa), the minimum strain is negative and the difference between the final and minimum strains is positive. For experiments that experienced only compaction ($\sigma_a \geq 3,553$ kPa) the minimum strain is negative and the difference between the final and minimum strains is 0. Vertical dashed lines located at $\sigma_a = 190$ kPa and $\sigma_a = 3,553$ kPa separate the three groups.

4.2. Experiments on Gypsum

In order to quantify the amount of creep in the product gypsum phase that can be expected in the bassanite hydration experiments, we performed two experiments on pure gypsum samples using the same procedures as for tests on bassanite samples (Figure 5). One experiment (G11) was performed at 12-kPa axial load that reached a final strain of about −0.4% after 45 hr, and another experiment (G12) was performed at ~2-MPa axial load and reached a final strain of about −5.3% after 174 hr. As expected both samples exhibit monotonic compaction, since there is no reaction occurring. The strain data in Figure 5 are overlain by theoretical predictions discussed in section 5.2.

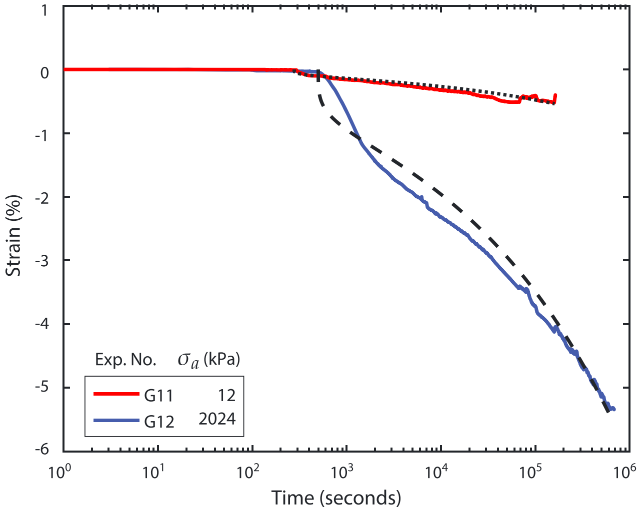

Figure 5. Axial strain data for gypsum creep experiments. The legend shows the experiment number by color. See Table 2 for parameters corresponding to each experiment. The dotted and dashed lines show strain predicted from equation (25), with grain sizes $d = 100$ μm and $d = 250$ μm, respectively, and appropriate values of σ_a.

5. Discussion

5.1. Factors Leading to Expansion Versus Compaction

The reaction and strain rates during bassanite hydration experiments depend on the availability of fluid and the applied load. Samples react and deform as water flows up the sample and infiltrates initially unsaturated bassanite. As the reaction proceeds, the porosity of the reacting region decreases, lowering permeability and affecting the infiltration rate, which also depends on the wetting behavior of the bassanite and gypsum grains comprising the porous skeleton (Scherer, 2004).

To aid in interpreting the experiments we can divide a hydrating sample into two regions: (1) the infiltration front and (2) the wetted region below the front. Deformation at the beginning of experiments is likely dominated by behavior at the infiltration front, since $\alpha = 0$ here and the reaction rate according to equation (2) will be faster than elsewhere. Eventually the infiltration front will reach the top of the sample, or some equilibrium height $h_r + h_p$, and stop moving, at which point deformation is due only to the behavior in the wetted region where α is nonzero and increasing and the reaction rate is slowing down.

An explanation for the general behavior of the experiments is that the relatively fast primary phase of deformation coincides with a moving infiltration front and the slower secondary phase begins when the movement of the infiltration front stops. About 1 g of water enters the most reacted samples over the course of an experiment, which equates to a drop in the water level of the pan by only ~50 μm. Our experimental setup does not allow for measurements of flow rates at this magnitude; thus, this hypothesis cannot be validated from the available data; however, it offers a simple explanation for the observed change in strain rates.

Further understanding of the experimental results can be gained by considering the volume change requirements for expansion to occur at a single grain contact. Local expansion will occur at a grain contact if the volume of gypsum precipitated there is larger than the volume of bassanite that dissolved. For example, if a given volume of bassanite dV_B dissolves at a grain contact, it can precipitate as gypsum with a volume of $dV_G = (V_{m,G}/V_{m,B})dV_B$, where $V_{m,G}$ and $V_{m,B}$ are the molar volumes of gypsum and bassanite. For zero strain to occur at this grain contact, a volume of gypsum equal to dV_B must precipitate there as opposed to in the pore space, which corresponds to $100 \times (V_{m,G} - V_{m,B})/V_{m,G} \approx 27\%$ of the total precipitated gypsum volume dV_G. Thus, the bulk sample behavior (compaction versus expansion) depends not only on the stoichiometry of the reaction but also on the porosity of the sample, and it is theoretically possible for the reaction to cause compaction even when the solid volume increases.

This calculation ignores many effects that can occur during dissolution/precipitation reactions in porous media, for example, the possibility of gypsum derived from dissolution of bassanite along pore walls precipitating in grain contacts. In addition, pressure solution creep can occur at gypsum grain contacts, causing further compaction. The net strain behavior results from the distribution of these processes throughout the entire sample, which in turn are controlled by reaction rates, movement of Ca^+ and SO_4^- ions through grain boundary fluid films and pore fluid as well as movement of the pore fluid itself, the local solubility of gypsum and bassanite, and the magnitude of the applied load. A sophisticated multiphysics model would be needed to evaluate the relative contribution of all these effects on the deformation behavior of hydrating porous materials (see Coussy, 2006; Malvoisin, Podladchikov, et al. 2017).

Monotonic expansion occurred at axial loads $\sigma_a \leq 150$ kPa (Figure 2, Samples B22, B27, B29, and B30). Since these samples expanded immediately, we can infer that net expansion occurred at the infiltration front as it moved up the sample. Precipitation in the pore space at the infiltration front likely also occurred, since the porosity of these samples reduced by 70–75% (Figure 3c). While it is difficult to identify a secondary deformation phase in the samples subjected to $\sigma_a = 12$ kPa, sample B28 ($\sigma_a = 150$ kPa) showed a clear transition from relatively fast expansion at early times to slower expansion toward the end of the experiment. The secondary, slow expansion phase in B28 can be explained by sufficient precipitation at grain contacts within the wetted region after the infiltration front had stopped moving and implies that expansion took place within the wetted zone while the infiltration front was moving as well.

At axial loads $\sigma_a \geq 230$ kPa, compaction occurred during the initial phase of deformation, implying that insufficient precipitation took place in grain contacts to cause net expansion within the infiltration front. At loads 230 kPa $\leq \sigma_a \leq 3.2$ MPa, secondary expansion took place after initial expansion, caused in the same manner as the secondary expansion described for sample B28. If at these loads the wetted region was expanding while the infiltration front was moving, then to result in net compaction it must have occurred at a slower integrated rate than compaction at the infiltration front. This seems to be the case, since when expansion occurred after initial compaction, it took place at a much slower rate. For axial loads $\sigma_a \geq 3.6$ MPa, secondary compaction (B32, $\sigma_a = 3.9$ MPa) or no deformation (B34, $\sigma_a = 3.6$ MPa) took place after initial compaction (Figure 4).

Figures 2 and 4 illustrate that there is a crystallization-induced stress $\sigma_c^{(i)}$ separating expansion from compaction in both the primary ($i = 1$) and secondary ($i = 2$) deformation phases. For the primary deformation phase $\sigma_c^{(1)}$ is constrained by experiments B27 and B28 so that 150 kPa $< \sigma_c^{(1)} <$ 230 kPa. For the secondary deformation phase the load is constrained by experiment B34 so that $\sigma_c^{(2)} = 3.6$ MPa. Accordingly with the previous discussion, the primary-phase crystallization-induced stress corresponds to conditions at the high porosity ($\phi \approx 0.3$), moving infiltration front, while the secondary-phase crystallization-induced stress corresponds to conditions in the lower porosity ($\phi \leq \sim 0.1$) wetted region. Aside from the differences in porosity, the order of magnitude discrepancy in these values might be explained by the presence of a liquid-vapor surface such as exists at the infiltration front and/or the local reaction extent.

As noted in section 2.2 and Table 1, the experimentally determined values of σ_c are 1–2 orders of magnitude smaller than the thermodynamically predicted value of the crystallization pressure Δp. Experimental studies on other reactions have found similar results. Wolterbeek et al. (2017) performed uniaxial deformation and hydration experiments on porous samples of calcium oxide (CaO) that were reacted with water to form portlandite [calcium hydroxide, $Ca(OH)_2$]. Following equation (6), they predicted a crystallization pressure of $\Delta p \approx 3.4$ GPa and observed a crystallization-induced stress of 153 MPa determined by a change from net expansion to net compaction. Wolterbeek et al. (2017) attributed the discrepancy to reaction-induced stresses closing fluid pathways and thus limiting reaction progress and stress buildup to GPa levels. The order of magnitude difference that we observed between $\sigma_c^{(1)}$ and $\sigma_c^{(2)}$ is consistent with a dependence of σ_c on the reaction extent, since α at the infiltration front should be much lower than in the wetted region. However, our results do not support the idea that limited reaction progress prevented $\sigma_c^{(2)}$ from approaching the crystallization pressure $\Delta p = 185$ MPa during secondary-phase deformation, since samples subjected to the highest loads reached reaction extents as large as 0.93 (Figure 3b).

5.2. Model for Strain as a Result of Solid Volume Increase and Gypsum Creep

To facilitate comparison between the bassanite hydration experiments, the strain after 40 hr is shown in Figure 6a as a function of the applied axial load. The experimental strains decrease nonlinearly with the logarithm of the axial load. These results can be explained by a phenomenological model for strain development due to a competition between reaction-induced volume expansion and compaction due to gypsum creep. To further simplify the analysis, we assume that the pore volume and grain contacts are saturated with pure water at all times. This amounts to ignoring fluid flow during the infiltration process and allows for characterization of the kinetics of the bassanite hydration reaction and gypsum creep using previously published empirical relationships.

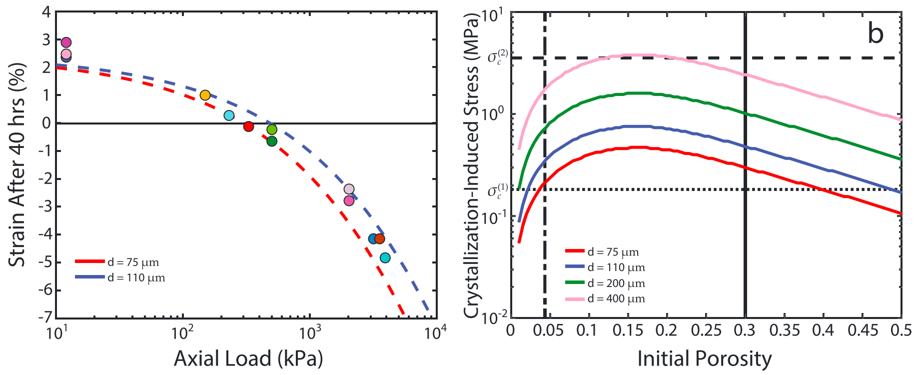

Figure 6. (a) Strain after 40 hr computed with h_i ($\sigma_a \leq 502$ kPa) and h_r^i ($\sigma_a \geq 2,024$ kPa) as a function of the applied axial load σ_a. Symbol colors are as in Figure 2. The dashed lines show predictions for grain sizes $d = 75$ μm (red) and $d = 110$ μm (blue). (b) Predicted crystallization-induced stress as a function of the initial porosity for grain sizes $d = 75$ μm (red), $d = 110$ μm (blue), $d = 200$ μm (green), and $d = 400$ μm (pink). The experimentally determined crystallization-induced stresses are shown by the horizontal dotted ($\sigma_c^{(1)} \approx 190$ kPa) and dashed ($\sigma_c^{(2)} \approx 3.6$ MPa) lines. The vertical lines show the experimental initial porosity (solid) and final porosity for B34, $\sigma_a \approx 3.6$ MPa (dash-dotted, $\phi_f = 0.043$).

In this section we develop equations for the net strain in a zero-dimensional system that considers dissolution of bassanite and concurrent precipitation of gypsum, which increases the solid and bulk volume. At the same time, we allow for a fraction of gypsum precipitation to "passively" decrease the pore volume, that is, this "pore invasion" does not change the bulk volume. We also allow for the pore and bulk volumes to decrease by compaction controlled by creep in the gypsum phase. This simple model is intended to illustrate how these competing volume-changing processes offer an explanation for the magnitude of reaction-induced stresses.

At any time, the total bulk volume $V_b(t)$ of the reacting system is equal to addition of the solid $V_s(t)$ and pore $V_p(t)$ volumes, and so the change in bulk volume is given by

$$\Delta V_b = \Delta V_s + \Delta V_p. \tag{13}$$

The change in solid volume is the addition of the change in bassanite volume ΔV_{B}, which is always negative, with the change in gypsum volume ΔV_{G}, which is always positive. We define a "pore invasion parameter" ξ, such that gypsum formation decreases the pore volume by $\xi \Delta V_{\mathrm{G}}$. The pore volume may also decrease from compaction by an amount ΔV_p^c. Substituting these considerations into equation (13) yields

$$\Delta V_b = \Delta V_p^c + \Delta V_{\mathrm{B}} + (1-\xi)\Delta V_{\mathrm{G}}, \tag{14}$$

again noting that ΔV_p^c, $\Delta V_{\mathrm{B}} < 0$, and $\Delta V_{\mathrm{G}} > 0$. These volume change considerations are shown schematically in Figure (7).

The changes in solid volume, ΔV_{G} and ΔV_{B}, depend on the reaction extent according to

$$\Delta V_{\mathrm{B}}(t) = -(1-\phi_i)V_b^i \alpha(t), \tag{15}$$

and

$$\Delta V_{\mathrm{G}}(t) = \left(\frac{V_{\mathrm{m,G}}}{V_{\mathrm{m,B}}}\right)(1-\phi_i)V_b^i \alpha(t), \tag{16}$$

where V_b^i is the initial bulk volume and $V_s^i = (1-\phi_i)V_b^i$ is the initial solid volume. Now the bulk strain, defined relative to V_b^i, may be written by substituting equations (15) and (16) into equation (14) and dividing by V_b^i, so that

$$\epsilon_b = \left[(1-\xi)\left(\frac{V_{\mathrm{m,G}}}{V_{\mathrm{m,B}}}\right) - 1\right](1-\phi_i)\alpha(t) + \epsilon_b^c, \tag{17}$$

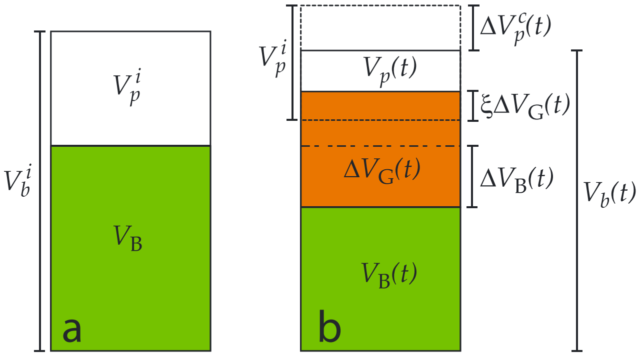

Figure 7. Schematic illustration of the volume change considerations described by equation (14). (a) Initial bulk volume V_b^i consists of bassanite V_B^i (green) and pore (white) volumes V_p^i. (b) At later times t, bassanite volume has decreased by $\Delta V_B(t)$ and gypsum volume (brown) has increased by $\Delta V_G(t)$. Some fraction ξ of the new gypsum has invaded the pore volume, which has been further reduced by $\Delta V_p^c(t)$ via compaction. The dashed box and dash-dot line indicate the extent of the initial pore and bassanite volumes, respectively.

where $\epsilon_b = \Delta V_b / V_b^i$ and $\epsilon_b^c = \Delta V_p^c / V_b^i$. Equation (17) is a statement that the total bulk strain ϵ_b is due to a combination of strain due to pore compaction ϵ_b^c and strain due to reaction-induced increases in solid volume, accounting for invasion of the pore volume. The bulk strain rate $\dot{\epsilon}_b$ is found by taking the derivative of equation (17) with respect to time and depends on both the reaction $\dot{\alpha}$ and compaction $\dot{\epsilon}_b^c$ rates, which will in turn both depend on the porosity.

The porosity at any time may be written as

$$\phi(t) = 1 - \frac{V_s(t)}{V_b(t)}. \tag{18}$$

Taking the derivative with respect to time yields

$$\frac{\partial \phi}{\partial t} = (1 - \phi) \left[\left(\frac{V_b^i}{V_b(t)} \right) \dot{\epsilon}_b - \left(\frac{V_s^i}{V_s(t)} \right) \dot{\epsilon}_s \right], \tag{19}$$

where the solid strain has been defined with respect to the initial solid volume. Expressions for all of the quantities within the square brackets are required to complete the formulation. There is an additional physical constraint in that both $\dot{\epsilon}_b$ and $\dot{\epsilon}_s$ must go to 0 as $\phi \to 0$, to ensure that $\dot{\phi}$ goes to 0 under the same limit. From equations (15) and (16), the solid strain rate is

$$\dot{\epsilon}_s = \frac{\Delta \dot{V}_s}{V_s^i} = \left(\frac{V_{m,G}}{V_{m,B}} - 1 \right) \dot{\alpha}(t), \tag{20}$$

and the bulk strain rate is found from equation (17). The current solid volume is given by

$$V_s(t) = \Delta V_s + V_s^i = \left[\left(\frac{V_{m,G}}{V_{m,B}} - 1 \right) \alpha(t) + 1 \right] V_s^i. \tag{21}$$

The current bulk volume is found from equations (15)–(17)

$$V_b(t) = \Delta V_b + V_b^i = \left\{ \left[(1 - \xi) \left(\frac{V_{m,G}}{V_{m,B}} \right) - 1 \right] (1 - \phi_i) \alpha(t) + \epsilon_b^c + 1 \right\} V_b^i, \tag{22}$$

again noting that $\epsilon_b^c < 0$. Finally, the porosity at any time may be written by inserting equations (21) and (22) into equation (18), so that

$$\phi(t) = 1 - \frac{1 + \left(\frac{V_{m,G}}{V_{m,B}} - 1 \right) \alpha(t)}{\frac{1+\epsilon_b^c}{1-\phi_i} + \left[(1 - \xi) \frac{V_{m,G}}{V_{m,B}} - 1 \right] \alpha(t)}. \tag{23}$$

The value of ξ can be estimated from experiments conducted with an axial load of 12 kPa (B22, B29, and B30). Based on the results of experiments on pure gypsum, we assume that a creep strain of 0.5% developed in the $\sigma_a = 12$-kPa bassanite experiments. Then equation (23) can be rearranged to solve for ξ using the final porosity and reaction extent from the experiments. The three experiments give an average value of $\xi = 0.24$. To simplify our calculations we assume this value for all values of σ_a.

It is important to emphasize that no assumptions regarding the applied stress state or internal sample structure are inherent in equations (13)–(23). These equations have been derived solely from considerations of volume changes in a reacting porous material. However, equation (17) indicates that an expression for the bulk compaction strain ϵ_b^c is needed to complete the formulation. The explicit dependence of ϵ_b^c on the applied stress state determines the appropriate conditions for the application of these equations.

We use equation (2) to determine the reaction extent at any time but modify it to include a linear dependence on porosity to mimic the effect of water supply on the reaction rate (e.g., Iyer et al., 2012), so that

$$\dot{\alpha} = K_\alpha \phi (1 - \alpha)^2. \tag{24}$$

To describe creep in the product gypsum phase we make use of the work of de Meer (1995), who found that the bulk strain rate due to uniaxial creep of wet gypsum can be described by an equation of the form

$$\dot{\epsilon} = \frac{A\sigma_a^2}{d^{2.5}\epsilon^3}, \tag{25}$$

where A is a constant equal to 4×10^{-33} and d is the grain size in meters. Equation (25) gives the strain rate due to compaction via decrease in the pore volume. In other words, since no reaction was involved in the experiments by de Meer (1995), there is no change in solid volume involved. Strain has been left without a subscript in equation (25), as it does not strictly apply to the model being developed here.

The power law dependence of strain rate on strain given by equation (25) was determined by fitting lines to log-log plots of strain rate versus strain. Because of this, although equation (25) predicts a decrease in porosity, it does not strictly depend on porosity in a theoretical sense and is an empirical formulation that does not produce physical behavior under limiting conditions. For example, $\dot{\epsilon} \to \infty$, as $\epsilon \to 0$, whereas a physical limit requires $\dot{\epsilon}$ to approach a constant value, or 0, under this limit. Likewise, for $\dot{\epsilon} \to 0$ in equation (25) one must have $\epsilon \to \infty$, where again a physical limit would have the strain rate approach 0 at some finite value of the strain. In the context of the model developed in this section, the unphysical limiting behavior will result in the development of negative values of porosity, since there is nothing in equation (25) preventing compaction from continuing as the pore volume is reduced to 0.

To circumvent this difficulty, we make an ad hoc change to equation (25) and assume that the strain rate due to compaction depends linearly on the porosity and that the dependence on ϵ^{-3} is replaced by $(\epsilon + \delta)^{-3}$, where δ is an arbitrarily small constant. In addition, since compaction depends on the presence of gypsum, none can occur until gypsum has formed. Thus, we make another ad hoc assumption that the compaction rate depends linearly on the reaction extent, so that

$$\dot{\epsilon}_b^c = \alpha\phi \left[\frac{A\sigma_a^2}{d^{2.5}(\epsilon_b^c + \delta)^3} \right]. \tag{26}$$

The strain in equation (26) is now identified as the strain due to compactive reduction in pore volume that appears in equations (17), (22), and (23). The additional dependencies on α and ϕ in equation (26) are not meant to rigorously represent any specific processes but only to produce physical limiting behavior when any of α, ϕ, and/or ϵ_b^c are equal to 0. These dependencies may certainly result in deviations from the true behavior of the reacting porous aggregates in our experiments. However, the modifications allow for the use of relevant experimental data and provide an illustration of how simultaneous compaction and expansion due to the reaction can affect crystallization-induced stresses. Finally, we set $\delta = -10^{-9}$, so that the strain rate predicted by equation (26) is always negative.

With $\alpha = 1$, equation (26) does a reasonably good job of reproducing the results of the experiments on pure gypsum that we performed (Figure 5). At an axial load of $\sigma_a = 12$ kPa the strain data are fit using a grain size of $d = 100$ µm, while for $\sigma_a = 2$ MPa a grain size of $d = 250$ µm is required. These grain sizes are within the range of initial grain sizes measured for the gypsum powder. The difference in grain sizes for the two axial loads is possibly due to a dependence of the water infiltration rate on the axial load but may also result in deviations of the true behavior from that described by equation (26).

The time derivative of equation (17) along with equations (22)–(24) and (26) form a coupled system of ordinary differential equations for ϕ, α, and ϵ_b^c. Examples of model results for $\sigma_a = 12$ kPa and $\sigma_a = 4$ MPa are shown in Figure S6. We solve these equations in MATLAB using a standard ODE integration scheme and find the bulk strain by inserting the computed values of α and ϵ_b^c into equation (17). Figure 6a shows the computed bulk strain after 40 hr for initial porosity $\phi_i = 0.3$ and gypsum grain sizes $d = 75$ and 110 μm. The smaller range of grain sizes relative to those used to fit the gypsum creep experiments may be due to the fact that gypsum grains have to nucleate and grow during the bassanite hydration experiments. Again, these differences in behavior may also be due to inaccuracies involved with equation (26).

Although the model reproduces the strain results after 40 hr, it does not reproduce the transitions from initial compaction to secondary expansion that occurred in the experiments. Reproducing this behavior likely requires a more sophisticated model that includes unsaturated fluid flow and the effects of a moving infiltration front. However, the crystallization-induced stress predicted by equations (23), (24), and (26) does depend strongly on the initial porosity and the grain size. Figure 6b shows the theoretical crystallization-induced stress for grain sizes $d = 75$, 110, 200, and 400 μm. For each line in Figure 6b, net expansion (compaction) occurs for axial loads in the region below (above) the line. The location of each line was determined by running a set of simulations with different initial porosities ϕ_i and axial loads σ_a, and for each value of ϕ_i, finding the value of σ_a where the strain after 40-hr transitions from net expansion to net compaction. For $d = 400$, the predicted crystallization-induced stress is close to $\sigma_c^{(2)}$ for initial porosities in the range $\phi_0 = 0.1–0.22$. Although the experimentally determined secondary-phase crystallization-induced stress was obtained for a final porosity of $\phi_f = 0.043$, the results of the simple model generally indicate that the crystallization-induced stress depends on the porosity in a manner similar to the experimental results.

5.3. Serpentinization

The good agreement that we obtain between our experimental and model results encourages application of a similar model for volume change due to serpentinization. The formation of serpentinite via hydration of olivine is an important process in a wide variety of geological settings, including in the alteration of oceanic lithosphere at mid-ocean ridges (Escartín et al., 1997a) and subduction zone forearcs (Hilairet et al., 2007), spheroidal weathering (Røyne et al., 2008), the geochemical cycling of volatiles (Kelemen et al., 2011), and in abiotic synthesis of organic compounds (McCollom et al., 2010).

The hydration of olivine can lead to a solid volume increase of 40–50% (Kelemen & Hirth, 2012). Reaction rates are highly dependent on the solid volume change (e.g., Malvoisin, Brantut, et al., 2017). If fluid pathways are clogged by reaction products, the reaction rate will tend toward 0. However, if the reaction generates stresses large enough to propagate fractures, fluid pathways will remain open and reaction rates will be relatively high. Large degrees of serpentinization are commonly observed in the field (Iyer et al., 2008; Macdonald & Fyfe, 1985) and can be reproduced by numerical models of olivine hydration that include fracturing processes (e.g., Malvoisin, Podladchikov, et al., 2017; Rudge et al., 2010). However, only a few experimental studies have observed reaction-induced fracturing during hydration reactions (Kuleci et al., 2017; Zhu et al., 2016) and attempts at measuring reaction-induced stresses due to olivine hydration or carbonation have met with limited success (Malvoisin & Brunet, 2014; van Noort et al., 2017).

Here we use the simple model outlined in the previous section and consider two representative reactions, one for the formation of lizardite [$Mg_3Si_2O_5(OH)_4$] and brucite [$Mg(OH)_2$] via hydration of forsterite olivine [Mg_2SiO_4] (e.g., Kelemen & Hirth, 2012)

$$2Mg_2SiO_4 + 3H_2O = Mg_3Si_2O_5(OH)_4 + Mg(OH)_2 \tag{27}$$

and one for the formation of antigorite [$Mg_{48}Si_{34}O_{85}(OH)_{62}$] via hydration of forsterite and enstatite [$Mg_2Si_2O_6$] (e.g., Ulmer & Trommsdorff, 1995)

$$14Mg_2SiO_4 + 10Mg_2Si_2O_6 + 31H_2O = Mg_{48}Si_{34}O_{85}(OH)_{62}. \tag{28}$$

Previously determined relations for the reaction rate and creep behavior of serpentinite allow for an estimate of confining pressures and temperatures where the reaction will lead to expansion or compaction. To interpret our results, we will make a simple assumption that expansion is necessary to generate fractures.

Malvoisin et al. (2012) determined a temperature- and grain size-dependent kinetic relation for lizardite formation, of the form (equations (A1) and (A2) in Malvoisin et al. (2012)

$$\dot{\alpha} = \left[\frac{nkf_1\phi}{(d/2)^{2n}}\right](1-\alpha), \tag{29}$$

where

$$f_1 = A\exp\left(-\frac{b}{T}\right)\left\{1-\exp\left[-c\left(\frac{1}{T}-\frac{1}{T_0}\right)\right]\right\}. \tag{30}$$

Malvoisin et al. (2012) provide a thorough discussion of equations (29) and (30). Parameter values are $A = 808.3$, $b = 3,640$ K, $c = 8,759$ K, and $T_0 = 623.6$ K is the equilibrium temperature above which the reaction will not proceed. The parameters n and k in equation (29) depend on grain size d, taking the values $(n,k) = (1.459, 0.008514)$ when $d = 5–15$ μm and $(n,k) = (1.289, 0.0133)$ or $(5.400, 8.561 \times 10^{-7})$ when $d = 50–63$ μm, depending on which pair of values gives the higher reaction extent as a function of time.

The only experimental study of antigorite formation was conducted by Eggler and Ehmann (2010). They determined the kinetics of reaction (28) at 2 GPa confining pressure and temperatures in the range 600–680°C, finding

$$\dot{\alpha} = \phi K_r A^i_\theta V_{\mathrm{m,Ant}}\left(\frac{T_{\mathrm{eq}}}{T}-1\right)(1-\alpha)^p), \tag{31}$$

where $K_r = 9.2\times10^{-12}$ mol·m^{-2}·s^{-1} is an empirical rate constant, A^i_θ is the initial specific surface area, $V_{\mathrm{m,Ant}} = 1.754\times10^{-3}$ m^3/mol is the molar volume of antigorite, $T_{\mathrm{eq}} = 6,432$°C is the equilibrium temperature of reaction (28) at 2 GPa, and p is a function of grain shape. For spherical grains $p = 2/3$ (Eggler & Ehmann, 2010) and $A^i_\theta = 6/d$ m^{-1}. We note that the value of K_r was incorrectly reported by Eggler and Ehmann (2010) as 9.2×10^{-11} mol·m^{-2}·s^{-1} due to a unit conversion error. As for equation (24), equations (29) and (31) are modified to include a linear dependence on porosity.

Amiguet et al. (2012) studied the creep behavior of lizardite at pressures of 1–8 GPa and temperatures of 150–400°C and found that their results were reasonably well described by flow laws for micas, so that creep strain rate depends on temperature and pressure as

$$\dot{\epsilon}_c = -C\alpha\phi\exp\left(\frac{\sigma}{0.41\mathrm{MPa}}-\frac{82\mathrm{kJ/mol}}{RT}\right), \tag{32}$$

where $C = 4.6\times10^{-6}$. The creep behavior of antigorite can be modeled using the results of Hilairet et al. (2007), who conducted deformation experiments at pressures of 1–4 GPa and temperatures of 200–500°C. Their strain rate data were best fit by a power law of the form

$$\dot{\epsilon}_c = -A\alpha\phi\sigma^n\exp\left[-\frac{8.9\mathrm{kJ/mol}+P_e\times3.2\mathrm{cm}^3/\mathrm{mol}}{RT}\right], \tag{33}$$

where P_e is the effective confining pressure and $A = 4\times10^{-38}$, $n = 3.8$.

Both equations (32) and (33) were determined from experiments on dense samples under conditions of applied differential stress. To incorporate them into our model formulation, equations (32) and (33) are modified as in equation (26) to include a linear dependence on both porosity and reaction extent. Multiplying the creep strain rates by porosity essentially results in volumetric creep laws, albeit ones likely prone to large errors. For example, the effect of porosity would be to intensify grain-scale stresses, likely leading to larger creep strain rates relative to dense samples. As for the application to our experimental results, the intent of these calculations it to illustrate how deformation in the product phase of a hydration reaction can potentially limit the magnitude of the crystallization-induced stresses. We maintain the simple linear dependence for simplicity, and note that higher creep strain rates would lead to even lower crystallization-induced stresses than are shown in the calculations below.

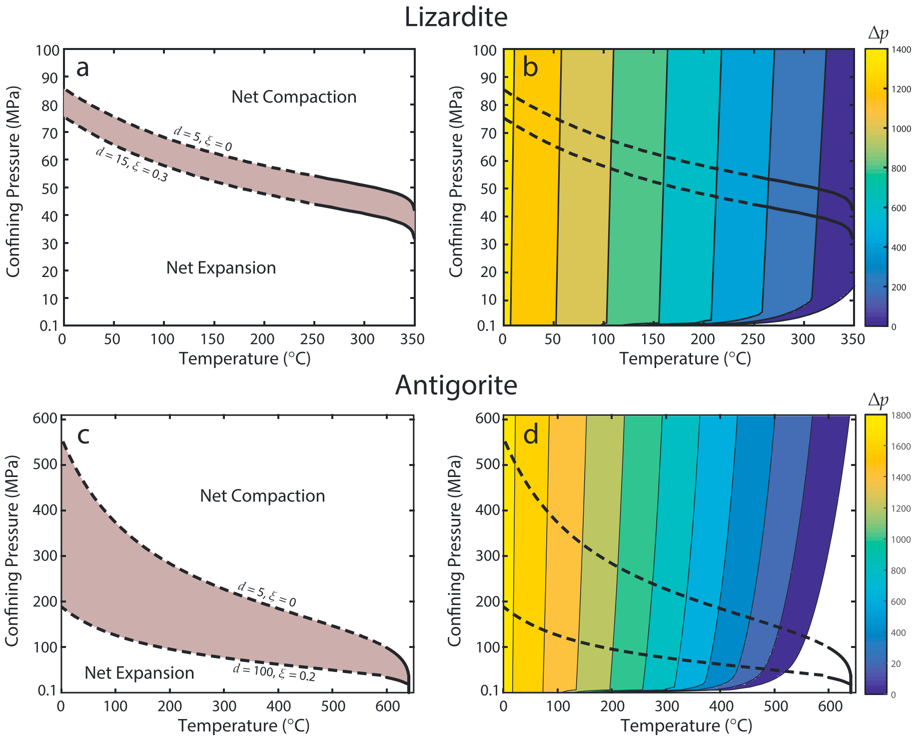

Figure 8. Results of expansion/compaction calculations for lizardite (a) and (b) and antigorite (c) and (d) formation. In panels (a) and (c) the boundaries between net compaction and net expansion are shown by the gray regions. Simulations resulted in net expansion (compaction) for values below (above) the gray band regardless of parameter values. Values of *d* and ξ used to determine the edges of the gray regions are indicated next to thick black lines. Solid black lines correspond to experimental temperatures from Malvoisin et al., 2012 (2012; panel a) and Eggler and Ehmann (2010; panel c). For all simulations $\phi_i = 0.01$. (a) Results for lizardite. The expansion/compaction boundary for simulations with $d = 63$ μm falls within the gray region. (b) Crystallization pressure for reaction (27). Heavy lines correspond to those in panel a. (c) Results for antigorite. All simulations with $\xi = 0.3$ resulted in net compaction regardless of temperature or confining pressure. (d) Crystallization pressure for reaction (28). Heavy black lines are as in panel (c).

We performed two sets of simulations: one for lizardite using equations (29), (30), and (32), along with equation (23) appropriately modified for reaction (27) (see Appendix A) and one for antigorite using equation (31) and equation (33), along with equation (23) modified for reaction (28). Each set of simulations produces a phase diagram that separates regions of net compaction from regions of net expansion as a function of confining pressure and temperature (Figure 8). Since the compaction rate equations (32) and (33) were determined for dense samples, we set the initial porosity to $\phi_i = 0.01$ for all simulations. We varied the values of the grain size from $d = 5$–63 μm for lizardite, from $d = 5$–100 μm for antigorite, and the value of the pore invasion parameter from 0 to 0.3 for each reaction, so that the boundary between compaction and expansion is an extended region in *P*-*T* space (gray regions in Figures 8a and 8c).

Simulations were run until the reaction stopped, either due to full conversion of the reactants or due to reduction of porosity to a vanishingly small value. For simulations that resulted in net expansion, the reaction extent is in the range 0.02–1, depending mainly on the value of ξ; reaction extents did not reach more than 0.02 in simulations with net compaction. In regions outside of the gray and red regions in Figures 8a and 8c, simulations predict net compaction or net expansion independent of the parameter values. Within these regions, the behavior depends on the values of *d* and ξ.

For lizardite, the compaction/expansion boundary is located at 75–85 MPa at 0°C and decreases to 30–40 MPa at 350°C (Figure 8a). For antigorite, the compaction/expansion boundaries occur at larger values of pressure (and over a larger range) relative to lizardite, for similar simulation parameters (Figure 8c). The compaction/expansion boundary is located at 200–550 MPa at 0°C and decreases to 0–37 MPa near the equilibrium temperature 642°C (Figure 8a). For lizardite, the decrease in the boundary stress with increasing temperature is due to the increase in the creep compaction strain rate in equation (32). Although the reaction rate increases with temperature as well, in this case the compaction rate is large enough to dominate the behavior. Similar behavior is observed in the antigorite calculation, although in this case the reaction rate monotonically decreases with temperature.

Figures 8b and 8d show the crystallization pressures for reactions (27) and (28) calculated using equation (6). Values were calculated using thermodynamic data from Holland and Powell (2011) for minerals and the equation of state for pure H_2O from Duan et al., 1992 (1992; see also Duan & Zhang, 2006; Kelemen & Hirth, 2012). For lizardite, aside from low-pressure, high-temperature conditions where ΔG becomes positive (lower right corner in Figure 8b), the crystallization pressure is greater than 100 MPa throughout most of the region where net expansion occurs and reaches values up to 1.4 GPa so that the confining pressure along most of the compaction/expansion boundary is about an order of magnitude lower than the corresponding crystallization pressure.

Lizardite is frequently observed at slow and ultraslow spreading ridges where serpentinized peridotites are observed to outcrop preferentially toward the end of spreading segments and in particular at the inside corner of ridge-offset intersections (Cannat et al., 1995; Escartín et al., 1997b; Tucholke & Lin, 1994). Estimates based on seismic velocities indicate that serpentinization likely occurs at depths up to 6 km at the Mid-Atlantic Ridge (Canales et al., 2000; Cannat et al., 2013). The confining pressures in the lizardite expansion field in Figure 8a correspond to depths up to 2–3 km, so the results of our simple model imply reaction-induced fracturing only in the shallowest regions.

For antigorite, the boundary between compaction and expansion falls well below 2 GPa, at values of confining pressure where the hydration of olivine and talc $[Mg_3Si_4O_{12}(OH)_2]$

$$18Mg_2SiO_4 + 4Mg_3Si_4O_{12}(OH)_2 + 27H_2O = Mg_{48}Si_{34}O_{85}(OH)_{62} \tag{34}$$

would be expected to take place rather than reaction (28) (Ulmer & Trommsdorff, 1995). We are not aware of any kinetic relations for the rate of reaction (34). Additionally, the kinetic relation for reaction (28) is only strictly valid for 2-GPa confining pressure and temperatures in the range 600° −642° . These considerations make interpretation of the antigorite calculation ambiguous. However, for the sake of discussion Figure 8d compares the calculated compaction/expansion boundary with the crystallization pressure of reaction (28). The values of confining pressure along the boundary are lower than the crystallization pressure by between an order of magnitude and a factor of 3.

6. Conclusion

Thermodynamic considerations indicate that large crystallization-induced stresses can be generated due to hydration reactions. We conducted uniaxial strain experiments on samples of reacting porous bassanite, under axial loads in the range 12 kPa $\leq \sigma_a \leq$ 3,928 kPa. The experiments generated crystallization-induced stresses no more than an order of magnitude less than the crystallization pressure $\Delta p = 185$ MPa.

At large porosities, when the reaction extent is small and the reaction rate is large, crystallization-induced stress occurred in the range $150 < \sigma_c^{(1)} < 230$ kPa. At lower porosities, when the reaction extent is larger and the reaction rate is slower, crystallization-induced stress reached $\sigma_c^{(2)} = 3.6$ MPa. The notion that reaction-induced stresses were limited by the strength of the porous aggregate is supported by the results of a simple numerical model that predicts strain due to the competing processes of solid volume increase and porosity reduction due to creep in gypsum. This model also predicts up to an order of magnitude increase in the induced stress with reduction of the initial porosity at the start of the reaction process.

The application of a similar model to the hydration of olivine similarly predicts crystallization-induced stresses about an order of magnitude lower than thermodynamically predicted crystallization pressures for both the formation of lizardite and antigorite. The mechanism leading to this reduction is the same as for the bassanite-gypsum model: pore compaction due to creep in the product serpentinite phase. For lizardite, the model predicts that net expansion, and by inference, induced cracking, due to the hydration reaction is limited to confining pressures less than 30–90 MPa, increasing with decreasing temperature.

Appendix A: Porosity Change for Simple Grain Contact Reaction Model

The porosity equation (23) must be appropriately modified to account for the stoichiometry of the serpentinization reactions considered in section 5.3. This amounts to properly writing the solid volume change ΔV_s

in terms of the reaction extent α, the molar volumes of the products and reactants, and the stoichiometric coefficients. For a general hydration reaction we can write

$$\sum_{\gamma} \nu_{\gamma} A_{\gamma} + \nu_{w} \mathrm{H_2O} = \sum_{\beta} \nu_{\beta} A_{\beta}, \tag{A1}$$

where ν are the stoichiometric coefficients with γ denoting reactants and β denoting products. The change in the volume of a given mineral participating in the reaction can be written in terms of the volume change of any other mineral, such that

$$\frac{\Delta V_{\gamma=\mathrm{i}}}{\nu_{\gamma=\mathrm{i}} V_{\mathrm{m},\gamma=\mathrm{i}}} = \frac{\Delta V_{\gamma}}{\nu_{\gamma} V_{\mathrm{m},\gamma}} = -\frac{\Delta V_{\beta}}{\nu_{\beta} V_{\mathrm{m},\beta}}, \tag{A2}$$

where $\gamma = \mathrm{i}$ denotes a specific reactant mineral and $V_{\mathrm{m},}$ denotes a molar volume. The solid volume change due to the reaction is

$$\Delta V_s = \sum_{\gamma} \Delta V_{\gamma} + \sum_{\beta} \Delta V_{\beta}, \tag{A3}$$

where by definition $\Delta V_{\gamma} < 0$ and $\Delta V_{\beta} > 0$. Making use of equation (A2), equation (A3) becomes

$$\Delta V_s = \frac{\Delta V_{\gamma=\mathrm{i}}}{\nu_{\gamma=\mathrm{i}} V_{\mathrm{m},\gamma=\mathrm{i}}} \left(\sum_{\gamma} \nu_{\gamma} V_{\mathrm{m},\gamma} - \sum_{\beta} \nu_{\beta} V_{\mathrm{m},\beta} \right). \tag{A4}$$

All of the quantities in equation (A4) are constants except for $\Delta V_{\gamma=\mathrm{i}}$, the change in volume for a specified reactant mineral. To complete the formulation, $\Delta V_{\gamma=\mathrm{i}}$ must be written in terms of the reaction extent $\alpha(t)$. If ϕ_{γ} is the fraction of the solid volume for each reactant at the start of the reaction, then

$$\Delta V_{\gamma} = -\phi_{\gamma} V_s^i \alpha, \tag{A5}$$

where V_s^i is the initial solid volume. If we assume that the initial volumes of the reactants are stoichiometrically balanced so that they are all exhausted when $\alpha = 1$, then the initial solid volume fraction of any specific reactant can be written as

$$\frac{\phi_{\gamma=\mathrm{i}}}{\nu_{\gamma=\mathrm{i}} V_{\mathrm{m},\gamma=\mathrm{i}}} = \frac{\phi_{\gamma}}{\nu_{\gamma} V_{\mathrm{m},\gamma}}. \tag{A6}$$

Along with the requirement that $\sum_{\gamma} \phi_{\gamma} = 1$, equation (A6) gives

$$\phi_{\gamma=\mathrm{i}} = \frac{\nu_{\gamma=\mathrm{i}} V_{\mathrm{m},\gamma=\mathrm{i}}}{\sum_{\gamma} \nu_{\gamma} V_{\mathrm{m},\gamma}}. \tag{A7}$$

Substituting equations (A5) and (A7) into equation (A4), the change in solid volume can now be written as

$$\Delta V_s = V_s^i \alpha(t) \left(\frac{\sum_{\beta} \nu_{\beta} V_{\mathrm{m},\beta}}{\sum_{\gamma} \nu_{\gamma} V_{\mathrm{m},\gamma}} - 1 \right). \tag{A8}$$

Similarly, the change in bulk volume due to the reaction can be written as

$$\Delta V_b^r = (1 - \xi) \sum_{\beta} \Delta V_{\beta} + \sum_{\gamma} \Delta V_{\gamma}, \tag{A9}$$

$$= V_s^i \alpha(t) \left[(1 - \xi) \left(\frac{\sum_{\beta} \nu_{\beta} V_{\mathrm{m},\beta}}{\sum_{\gamma} \nu_{\gamma} V_{\mathrm{m},\gamma}} \right) - 1 \right]. \tag{A10}$$

Equations (A8) and (A10) can be used to write the porosity as a function of the reaction extent, for any reaction, where

$$\phi(t) = 1 - \frac{V_s(t)}{V_b(t)} = 1 - \frac{V_s^i + \Delta V_s(t)}{V_b^i + \Delta V_b^r + \Delta V_b^c}. \tag{A11}$$

Noting that $V_s^i = (1 - \phi_i)V_b^i$ and $\Delta V_b^c = \epsilon_c V_b^i$, the final form of the porosity equation that we use is

$$\phi(t) = 1 - \frac{1 + \left(\frac{\sum_\beta \nu_\beta V_{\mathrm{m},\beta}}{\sum_\gamma \nu_\gamma V_{\mathrm{m},\gamma}} - 1 \right) \alpha(t)}{\frac{1+\epsilon_c}{1-\phi_i} + \left[(1 - \xi) \left(\frac{\sum_\beta \nu_\beta V_{\mathrm{m},\beta}}{\sum_\gamma \nu_\gamma V_{\mathrm{m},\gamma}} \right) - 1 \right] \alpha(t)}. \tag{A12}$$

Acknowledgments
The authors would like to thank Ted Koczynski and Reinhard Kozdon for helpful laboratory assistance. This work was supported by NSF grant EAR 15-20732. All data generated by this work are contained in Table 2 and Data Set S1.

References

Amiguet, E., Reynard, B., Caracas, R., de Moortèle, B. V., Hilairet, N., & Wang, Y. (2012). Creep of phyllosilicates at the onset of plate tectonics. *Earth and Planetary Science Letters*, *345-348*, 142–150. https://doi.org/10.1016/j.epsl.2012.06.033

Anagnostou, G., Pimentel, E., & Serafeimidis, K. (2010). Swelling of sulphatic claystones—Some fundamental questions and their practical relevance. *Geomechanics and Tunnelling*, *3*(5), 567–572. https://doi.org/10.1002/geot.201000033

Azimi, G., Papangelakis, V., & Dutrizac, J. (2007). Modelling of calcium sulphate solubility in concentrated multi-component sulphate solutions. *Fluid Phase Equilibria*, *260*(2), 300–315. https://doi.org/10.1016/j.fluid.2007.07.069

Bedford, J. D., Faulkner, D. R., Leclere, H., & Wheeler, J. (2018). High-resolution mapping of yield curve shape and evolution for porous rock: The effect of inelastic compaction on porous bassanite. *Journal of Geophysical Research: Solid Earth*, *123*, 1217–1234. https://doi.org/10.1002/2017JB015250

Brantut, N., Schubnel, A., David, E. C., Héripré, E., Guéguen, Y., & Dimanov, A. (2012). Dehydration-induced damage and deformation in gypsum and implications for subduction zone processes. *Journal of Geophysical Research*, *117*, b03205. https://doi.org/10.1029/2011JB008730

Canales, J. P., Collins, J. A., Escartín, J., & Detrick, R. S. (2000). Seismic structure across the rift valley of the Mid-Atlantic Ridge at 23°20′ (MARK area): Implications for crustal accretion processes at slow spreading ridges. *Journal of Geophysical Research*, *105*(B12), 28,411–28,425. https://doi.org/10.1029/2000JB900301

Cannat, M., Fontaine, F., & Escartín, J. (2013). Serpentinization and Associated Hydrogen And Methane Fluxes at Slow Spreading Ridges. In P. A. Rona, C. W. Devey, J. Dyment, & B. J. Murton (Eds.), *Diversity Of Hydrothermal Systems On Slow Spreading Ocean Ridges* (pp. 241–264). Washington, DC: American Geophysical Union. https://doi.org/10.1029/2008GM000760

Cannat, M., Mevel, C., Maia, M., Deplus, C., Durand, C., Gente, P., et al. (1995). Thin crust, ultramafic exposures, and rugged faulting patterns at the Mid-Atlantic Ridge (22°–24° N). *Geology*, *23*(1), 49–52. https://doi.org/10.1130/0091-7613(1995)023<0049:TCUEAR>2.3.CO;2

Carlson, J. E., & Taavitsainen, V.-M. (2008). Ultrasonic measurement of the reaction kinetics of the setting of calcium sulfate cements using implicit calibration. *Journal of Chemometrics*, *22*(11-12), 752–757. https://doi.org/10.1002/cem.1136

Charola, A. E., Pühringer, J., & Steiger, M. (2007). Gypsum: A review of its role in the deterioration of building materials. *Environmental Geology*, *52*(2), 339–352. https://doi.org/10.1007/s00254-006-0566-9

Comel, C., Karmazsin, E., & Murat, M. (1979). Theoretical interpretation of the existence at 35°C of an absolute maximum of the hydration rate of calcium sulfate hemihydrate. *Thermochimica Acta*, *31*(1), 71–77. https://doi.org/10.1016/0040-6031(79)80009-X

Correns, C. W. (1949). Growth and dissolution of crystals under linear pressure. *Discussions of the Faraday Society*, *5*, 267–271. https://doi.org/10.1039/DF9490500267

Coussy, O. (2006). Deformation and stress from in-pore drying-induced crystallization of salt. *Journal of the Mechanics and Physics of Solids*, *54*(8), 1517–1547. https://doi.org/10.1016/j.jmps.2006.03.002

de Boer, R. B. (1977). On the thermodynamics of pressure solution: Interaction between chemical and mechanical forces. *Geochimica et Cosmochimica Acta*, *41*(2), 249–256. https://doi.org/10.1016/0016-7037(77)90232-0

de Meer, S. (1995). Deformation processes in polycrystalline aggregates of gypsum (PhD thesis, vol.132), Utrecht University.

Derjaguin, B. V. (1987). Some results from 50 years' research on surface forces, *Surface forces and surfactant systems* (pp. 17–30). Darmstadt: Steinkopff. https://doi.org/10.1007/BFb0109369

Duan, Z., Møller, N., & Weare, J. H. (1992). An equation of state for the CH_4-CO_2-H_2O system: I. Pure systems from 0 to 1000°C and 0 to 8000 bar. *Geochimica et Cosmochimica Acta*, *56*(7), 2605–2617. https://doi.org/10.1016/0016-7037(92)90347-L

Duan, Z., & Zhang, Z. (2006). Equation of state of the H_2O, CO_2, and H_2O-CO_2 systems up to 10 GPa and 2573.15 K: Molecular dynamics simulations with ab initio potential surface. *Geochimica et Cosmochimica Acta*, *70*(9), 2311–2324. https://doi.org/10.1016/j.gca.2006.02.009

Eggler, D. H., & Ehmann, A. N. (2010). Rate of antigorite dehydration at 2 GPa applied to subduction zones. *American Mineralogist*, *95*(5-6), 761–769. https://doi.org/10.2138/am.2010.3227

Escartín, J., Hirth, G., & Evans, B. (1997a). Effects of serpentinization on the lithospheric strength and the style of normal faulting at slow-spreading ridges. *Earth and Planetary Science Letters*, *151*(3), 181–189. https://doi.org/10.1016/S0012-821X(97)81847-X

Escartín, J., Hirth, G., & Evans, B. (1997b). Nondilatant brittle deformation of serpentinites: Implications for Mohr-Coulomb theory and the strength of faults. *Journal of Geophysical Research*, *102*(B2), 2897–2913. https://doi.org/10.1029/96JB02792

Espinosa-Marzal, R. M., & Scherer, G. W. (2010). Advances in understanding damage by salt crystallization. *Accounts of Chemical Research*, *43*(6), 897–905. https://doi.org/10.1021/ar9002224

Flatt, R. J. (2002). Salt damage in porous materials: How high supersaturations are generated. *Journal of Crystal Growth*, *242*(3), 435–454. https://doi.org/10.1016/S0022-0248(02)01429-X

Flatt, R. J., Steiger, M., & Scherer, G. W. (2007). A commented translation of the paper by CW Correns and W. Steinborn on crystallization pressure. *Environmental Geology*, *52*(2), 187. https://doi.org/10.1007/s00254-006-0509-5

Fujii, K., & Kondo, W. (1986). Kinetics of hydration of calcium sulphate hemihydrate. *Journal of the Chemical Society, Dalton Transactions*, *24*, 729–731. https://doi.org/10.1039/DT9860000729

Ghofrani, R., & Plack, H. (1993). *CaO- and/or MgO-swelling cements: A key for providing a better annular sealing? SPE/IADC drilling conference*. Amsterdam, Netherlands: Society of Petroleum Engineers. https://doi.org/10.2118/25697-MS

Gonçalvès, J., Rousseau-Gueutin, P., de Marsily, G., Cosenza, P., & Violette, S. (2010). What is the significance of pore pressure in a saturated shale layer? *Water Resources Research*, *46*, w04514. https://doi.org/10.1029/2009WR008090

Hand, R. (1994). The kinetics of hydration of calcium sulphate hemihydrate: A critical comparison of the models in the literature. *Cement and Concrete Research*, *24*(5), 885–895. https://doi.org/10.1016/0008-8846(94)90008-6

Hand, R. (1997). Calcium sulphate hydrates: A review. *British Ceramic Transactions*, *96*(3), 116–120.

Heard, H. C., & Rubey, W. W. (1966). Tectonic implications of gypsum dehydration. *GSA Bulletin*, *77*(7), 741–760. https://doi.org/10.1130/0016-7606(1966)77[741:TIOGD]2.0.CO;2

Hilairet, N., Reynard, B., Wang, Y., Daniel, I., Merkel, S., Nishiyama, N., & Petitgirard, S. (2007). High-pressure creep of serpentine, interseismic deformation, and initiation of subduction. *Science*, *318*(5858), 1910–1913. https://doi.org/10.1126/science.1148494

Holland, T. J. B., & Powell, R. (2011). An improved and extended internally consistent thermodynamic dataset for phases of petrological interest, involving a new equation of state for solids. *Journal of Metamorphic Geology*, *29*(3), 333–383. https://doi.org/10.1111/j.1525-1314.2010.00923.x

Iyer, K., Jamtveit, B., Mathiesen, J., Malthe-Sørenssen, A., & Feder, J. (2008). Reaction-assisted hierarchical fracturing during serpentinization. *Earth and Planetary Science Letters*, *267*(3), 503–516. https://doi.org/10.1016/j.epsl.2007.11.060

Iyer, K., Rüpke, L. H., Phipps Morgan, J., & Grevemeyer, I. (2012). Controls of faulting and reaction kinetics on serpentinization and double Benioff zones. *Geochemistry, Geophysics, Geosystems*, *13*, Q09010. https://doi.org/10.1029/2012GC004304

Kelemen, P. B., & Hirth, G. (2012). Reaction-driven cracking during retrograde metamorphism: Olivine hydration and carbonation. *Earth and Planetary Science Letters*, *345*, 81–89. https://doi.org/10.1016/j.epsl.2012.06.018

Kelemen, P. B., & Matter, J. (2008). In situ carbonation of peridotite for CO_2 storage. *Proceedings of the National Academy of Sciences of the United States of America*, *105*(45), 17,295–17,300. https://doi.org/10.1073/pnas.0805794105

Kelemen, P. B., Matter, J., Streit, E. E., Rudge, J. F., Curry, W. B., & Blusztajn, J. (2011). Rates and mechanisms of mineral carbonation in peridotite: Natural processes and recipes for enhanced, in situ CO_2 capture and storage. *Annual Review of Earth and Planetary Sciences*, *39*(1), 545–576. https://doi.org/10.1146/annurev-earth-092010-152509

Kuleci, H., Ulven, O., Rybacki, E., Wunder, B., & Abart, R. (2017). Reaction-induced fracturing in a hot pressed calcite-periclase aggregate. *Journal of Structural Geology*, *94*, 116–135. https://doi.org/10.1016/j.jsg.2016.11.009

Li, K. (2017). *Durability design of concrete structures: Phenomena, modeling, and practice*. Singapore: John Wiley.

Llana-Fúnez, S., Wheeler, J., & Faulkner, D. R. (2012). Metamorphic reaction rate controlled by fluid pressure not confining pressure: Implications of dehydration experiments with gypsum. *Contributions to Mineralogy and Petrology*, *164*(1), 69–79. https://doi.org/10.1007/s00410-012-0726-8

Macdonald, A., & Fyfe, W. (1985). Rate of serpentinization in seafloor environments. *Tectonophysics*, *116*(1), 123–135. https://doi.org/10.1016/0040-1951(85)90225-2

Malvoisin, B., Brantut, N., & Kaczmarek, M.-A. (2017). Control of serpentinisation rate by reaction-induced cracking. *Earth and Planetary Science Letters*, *476*, 143–152. https://doi.org/10.1016/j.epsl.2017.07.042

Malvoisin, B., & Brunet, F. (2014). Water diffusion-transport in a synthetic dunite: Consequences for oceanic peridotite serpentinization. *Earth and Planetary Science Letters*, *403*, 263–272. https://doi.org/10.1016/j.epsl.2014.07.004

Malvoisin, B., Brunet, F., Carlut, J., Rouméjon, S., & Cannat, M. (2012). Serpentinization of oceanic peridotites: 2. Kinetics and processes of San Carlos olivine hydrothermal alteration. *Journal of Geophysical Research*, *117*, B04102. https://doi.org/10.1029/2011JB008842

Malvoisin, B., Podladchikov, Y. Y., & Vrijmoed, J. C. (2017). Coupling changes in densities and porosity to fluid pressure variations in reactive porous fluid flow: Local thermodynamic equilibrium. *Geochemistry, Geophysics, Geosystems*, *16*, 4362–4387. https://doi.org/10.1002/2015GC006019

Marčelja, S., & Radiá, N. (1976). Repulsion of interfaces due to boundary water. *Chemical Physics Letters*, *42*(1), 129–130. https://doi.org/10.1016/0009-2614(76)80567-2

Matter, J. M., & Kelemen, P. B. (2009). Permanent storage of carbon dioxide in geological reservoirs by mineral carbonation. *Nature Geoscience*, *2*(12), 837. https://doi.org/10.1038/ngeo683

McCollom, T. M., Lollar, B. S., Lacrampe-Couloume, G., & Seewald, J. S. (2010). The influence of carbon source on abiotic organic synthesis and carbon isotope fractionation under hydrothermal conditions. *Geochimica et Cosmochimica Acta*, *74*(9), 2717–2740. https://doi.org/10.1016/j.gca.2010.02.008

Noiriel, C., Renard, F., Doan, M.-L., & Gratier, J.-P. (2010). Intense fracturing and fracture sealing induced by mineral growth in porous rocks. *Chemical Geology*, *269*(3), 197–209. https://doi.org/10.1016/j.chemgeo.2009.09.018

Novak, G. A., & Colville, A. A. (1989). Efflorescent mineral assemblages associated with cracked and degraded residential concrete foundations in Southern California. *Cement and Concrete Research*, *19*(1), 1–6. https://doi.org/10.1016/0008-8846(89)90059-8

Ostapenko, G. T. (1976). Excess pressure on the solid phases generated by hydration (according to experimental data on hydration of periclase). *Geochemistry International*, *13*(3), 120–138.

Ostapenko, G. T., & Yaroshenko, N. S. (1975). Excess pressure on solid phases generated by hydration (experimental data on hydration of plaster of Paris and lime). *Geochemistry International*, *12*, 72–81.

Putnis, A. (2009). Mineral replacement reactions. *Reviews in Mineralogy and Geochemistry*, *70*(1), 87–124. https://doi.org/10.2138/rmg.2009.70.3

Putnis, A. (2015). Transient porosity resulting from fluid-mineral interaction and its consequences. *Reviews in Mineralogy and Geochemistry*, *80*(1), 1–23. https://doi.org/10.2138/rmg.2015.80.01

Ridge, M. J., King, G. A., & Molony, B. (1972). Reconsideration of a theory of the setting of gypsum plaster. *Journal of Chemical Technology & Biotechnology*, *22*(10), 1065–1075. https://doi.org/10.1002/jctb.5020221005

Rousseau-Gueutin, P., de Greef, V., Gonçalvès, J., Violette, S., & Chanchole, S. (2009). Experimental device for chemical osmosis measurement on natural clay-rock samples maintained at in situ conditions: Implications for formation pressure interpretations. *Journal of Colloid and Interface Science*, *337*(1), 106–116. https://doi.org/10.1016/j.jcis.2009.04.092

Røyne, A., Jamtveit, B., Mathiesen, J., & Malthe-Sørenssen, A. (2008). Controls on rock weathering rates by reaction-induced hierarchical fracturing. *Earth and Planetary Science Letters*, *275*(3), 364–369. https://doi.org/10.1016/j.epsl.2008.08.035

Rudge, J. F., Kelemen, P. B., & Spiegelman, M. (2010). A simple model of reaction-induced cracking applied to serpentinization and carbonation of peridotite. *Earth and Planetary Science Letters*, *291*(1), 215–227. https://doi.org/10.1016/j.epsl.2010.01.016

Scherer, G. W. (1999). Crystallization in pores. *Cement and Concrete Research*, *29*(8), 1347–1358. https://doi.org/10.1016/S0008-8846(99)00002-2

Scherer, G. (2000). Stress from crystallization of salt in pores. In V. Fassina (Ed.), *Proc. 9th Int. Cong. Deterioration and Conservation of Stone*, (Vol. 1, pp. 187–194). Amsterdam: Elsevier.

Scherer, G. W. (2004). Stress from crystallization of salt. *Cement and Concrete Research*, *34*(9), 1613–1624. https://doi.org/10.1016/j.cemconres.2003.12.034

Schiller, K. (1974). The course of hydration: Its practical importance and theoretical interpretation. *Journal of Chemical Technology & Biotechnology*, *24*(7), 379–385. https://doi.org/10.1002/jctb.2720240702

Serafeimidis, K., & Anagnostou, G. (2014). On the crystallisation pressure of gypsum. *Environmental Earth Sciences*, *72*(12), 4985–4994. https://doi.org/10.1007/s12665-014-3366-7

Singh, N., & Middendorf, B. (2007). Calcium sulphate hemihydrate hydration leading to gypsum crystallization. *Progress in Crystal Growth and Characterization of Materials*, *53*(1), 57–77. https://doi.org/10.1016/j.pcrysgrow.2007.01.002

Steiger, M. (2005a). Crystal growth in porous materials–I: The crystallization pressure of large crystals. *Journal of Crystal Growth*, *282*(3), 455–469. https://doi.org/10.1016/j.jcrysgro.2005.05.007

Steiger, M. (2005b). Crystal growth in porous materials–II: Influence of crystal size on the crystallization pressure. *Journal of Crystal Growth*, *282*(3), 470–481. https://doi.org/10.1016/j.jcrysgro.2005.05.008

Tsui, N., Flatt, R. J., & Scherer, G. W. (2003). Crystallization damage by sodium sulfate. *Journal of Cultural Heritage*, *4*(2), 109–115. https://doi.org/10.1016/S1296-2074(03)00022-0

Tucholke, B. E., & Lin, J. (1994). A geological model for the structure of ridge segments in slow spreading ocean crust. *Journal of Geophysical Research*, *99*(B6), 11,937–11,958. https://doi.org/10.1029/94JB00338

Ulmer, P., & Trommsdorff, V. (1995). Serpentine stability to mantle depths and subduction-related magmatism. *Science*, *268*(5212), 858–861.

Van Driessche, A. E. S., Stawski, T. M., Benning, L. G., & Kellermeier, M. (2017). Calcium sulfate precipitation throughout its phase diagram. In A. Van Driessche, M. Kellermeier, L. Benning, & D. Gebauer (Eds.), *New perspectives on mineral nucleation and growth* (pp. 227–256). Cham: Springer. https://doi.org/10.1007/978-3-319-45669-0_12

van Noort, R., Wolterbeek, T. K. T., Drury, M. R., Kandianis, M. T., & Spiers, C. J. (2017). The force of crystallization and fracture propagation during in-situ carbonation of peridotite. *Minerals*, *7*(10). https://doi.org/10.3390/min7100190

Van Rosmalen, G. M., Daudey, P., & Marchée, W. (1981). An analysis of growth experiments of gypsum crystals in suspension. *Journal of Crystal Growth*, *52*(Part 2), 801–811. https://doi.org/10.1016/0022-0248(81)90379-1

Warren, J. K. (2006). *Evaporites: Sediments, resources and hydrocarbons*. Springer Science & Business Media.

Weyl, P. K. (1959). Pressure solution and the force of crystallization: A phenomenological theory. *Journal of Geophysical Research*, *64*(11), 2001–2025. https://doi.org/10.1029/JZ064i011p02001

Wolterbeek, T. K. T., van Noort, R., & Spiers, C. J. (2017). Reaction-driven casing expansion: Potential for wellbore leakage mitigation. *Acta Geotechnica*, *13*(2), 341–366. https://doi.org/10.1007/s11440-017-0533-5

Wong, T.-F., Ko, S.-C., & Olgaard, D. L. (1997). Generation and maintenance of pore pressure excess in a dehydrating system 2. Theoretical analysis. *Journal of Geophysical Research*, *102*(B1), 841–852. https://doi.org/10.1029/96JB02484

Zhu, W., Fusseis, F., Lisabeth, H., Xing, T., Xiao, X., De Andrade, V., & Karato, S.-i. (2016). Experimental evidence of reaction-induced fracturing during olivine carbonation. *Geophysical Research Letters*, *43*, 9535–9543. https://doi.org/10.1002/2016GL070834